land

MDPI

Article

Integrated Geomechanical and Digital Photogrammetric Survey in the Study of Slope Instability Processes of a Flysch Sea Cliff (Debeli Rtič Promontory, Slovenia)

Stefano Furlani [1], Alberto Bolla [2,*], Linley Hastewell [3], Matteo Mantovani [4] and Stefano Devoto [1]

[1] Department of Mathematics and Geosciences, University of Trieste, 34127 Trieste, Italy
[2] Polytechnic Department of Engineering and Architecture, University of Udine, 33100 Udine, Italy
[3] School of the Environment, Geography and Geosciences, University of Portsmouth, Portsmouth PO1 3HE, UK
[4] National Research Council of Italy (CNR), Research Institute for Geo-Hydrological Protection (IRPI), 35127 Padova, Italy
* Correspondence: alberto.bolla@uniud.it; Tel.: +39-0432-558738

Abstract: This work presents an integrated study approach that combines the results of a geomechanical survey with data obtained using digital photogrammetry (DP), to assess slope instability processes affecting a sea cliff at the Debeli Rtič promontory (Slovenia). The investigated cliff is 4–18 m-high and is made up of an alternation of sandstones and marlstones belonging to the Flysch Formation of Trieste, which is Eocene in age. The studied cliff was subjected to localized slope failures that occurred in the past and is currently subject to frequent rock collapses, thus resulting in its partial and episodic retreat. Field evidence acquired through a traditional survey was integrated with outputs of the DP technique based on 1399 images that were collected using both a commercial unmanned aerial vehicle (UAV) and a mobile phone (MP). UAV-derived images were useful for performing rock mass structure analysis in the upper part of the investigated cliff, where the traditional survey was not possible due to hazardous operating conditions. In addition, the use of a MP was observed to be a useful tool for the rapid collection of images at the toe of unsafe marine cliff environments. This study highlights that UAV-DP and MP-DP techniques can only be effective if the outcomes obtained from the 3D model reconstruction are validated by direct measurements acquired by means of the traditional field survey, thus avoiding improper or even erroneous results while enlarging the amount of data and the area of investigation. The study approach presented herein allowed for the assessment of slope instabilities affecting the Flysch Sea cliff, whose retreat is caused by the combined action of marine erosion and slope gravitational processes.

Keywords: rocky coast; sea cliff retreat; field survey; UAV; mobile phone; Mediterranean Sea

Citation: Furlani, S.; Bolla, A.; Hastewell, L.; Mantovani, M.; Devoto, S. Integrated Geomechanical and Digital Photogrammetric Survey in the Study of Slope Instability Processes of a Flysch Sea Cliff (Debeli Rtič Promontory, Slovenia). *Land* **2022**, *11*, 2255. https://doi.org/10.3390/land11122255

Academic Editors: Candide Lissak, Christopher Gomez and Vittoria Vandelli

Received: 14 November 2022
Accepted: 8 December 2022
Published: 10 December 2022

1. Introduction

Sea cliffs exist on approximately 80% of the global shoreline [1], so they represent a fundamental, and widely distributed coastal morphotype. Sea cliffs most probably constitute the dominant landform of the so-called "rocky coasts". Furlani et al. [2] mapped rocky coasts in the Mediterranean and Black Seas, reviewing all previous studies in the area. Sea cliffs are often divided into "soft" and "hard" rocky coasts, depending on the lithological features of the coast. According to the Eurosion project classification, combined "soft" and "hard" rock categories comprise 47% of the European coasts, as reported by [3]. Sea cliffs can be subject to instability processes characterized by slope failures that result in progressive cliff retreat, occasionally causing damage to coastal infrastructure and even fatalities [4,5]. In the eastern part of the Gulf of Trieste (GOT), sea cliffs made up of terrigenous sequences with shore platforms at the slope toe constitute the dominant morphotype [6]. In this area, sea cliff retreat generates wide shore platforms without a marked seaward drop, due to sea level change and the local tectonic setting [7]. The sea cliff

retreat of the Slovenian coast is the result of both marine and subaerial processes. Lithology and sea conditions also play a key role in the evolution of these coastal features [8].

To properly assess the instability processes affecting a rocky coast, including the evaluation of the failure hazard of unstable rock masses, the analysis of the rock mass arrangement and orientation of discontinuities is mandatory. The traditional geomechanical survey allows for the acquisition of direct measurements from accessible rock outcrops. However, field procedures for data acquisition are time-consuming, and often require the selection of surveyed outcrops that are considered small relative to the total extent of the area under investigation, thus providing data samples of a limited size. In addition, under some circumstances, key rock outcrops are often inaccessible unless using climbing techniques, which result in an additional health and safety risk [9]. To overcome these limitations, recent research developments have demonstrated the effective use of a Remote Sensing (RS) approach to identify the structural features of a rock mass, particularly for inaccessible outcrops and/or areas where field conditions are considered dangerous [10–13]. Among the various RS techniques, the DP image processing methodology is widely used to build measurable 3D models based on a large number of photos obtained using a UAV camera and/or a MP. Although UAV has largely proven to be efficient for image collection in rock slope stability problems e.g., [14–16], a MP is increasingly used for scientific purposes [17], specifically for field applications through mobile apps built for geological field surveys, or dedicated sensors, such as iPhone Lidar e.g., [18–20]. To date, no research has been published to evaluate the possibility of successfully using MP devices for the study of sea cliff instabilities. In this respect, the integration of RS datasets and field outputs represents a challenging task in terms of assessing methods and approaches aimed at acquiring extensive and reliable data following safe procedures.

The main aim of this study is to integrate data acquired through a traditional geomechanical survey with information obtained from UAV-DP and MP-DP outputs (i.e., point clouds and 3D models) to investigate the rock mass arrangement and orientation data of rock joints. These procedures were tested along the west and south sectors of a Slovenian promontory named Debeli Rtič (Figure 1). The Debeli Rtič case study was selected owing to the considerable sea cliff retreat rate, which results in a considerable hydrogeological risk. Furthermore, a large number of images from the site (more than 10,000) have been collected since 1998 that allow for a detailed assessment of the area's geomorphological evolution. The findings of the analyses will further contribute to the assessment of sea cliff instabilities and associated hazards.

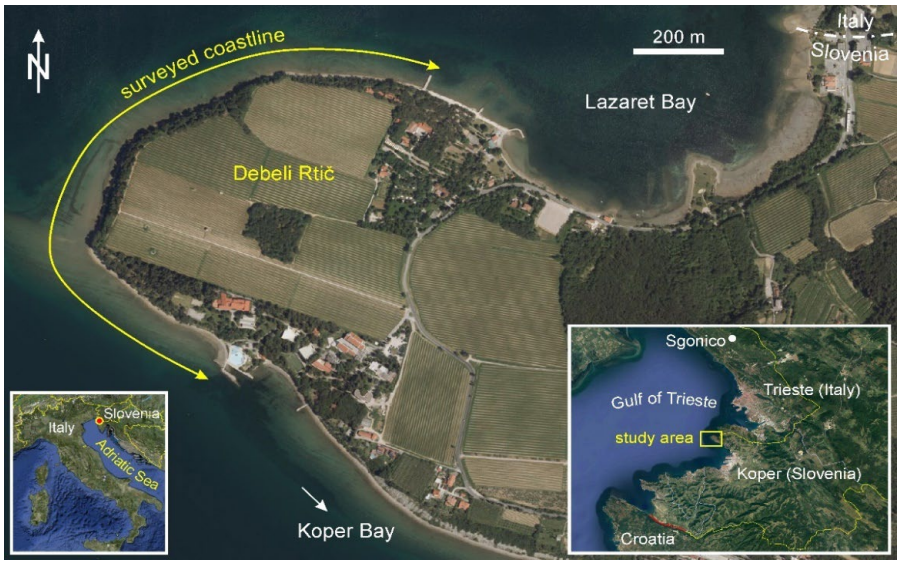

Figure 1. Location of the Debeli Rtič promontory. The surveyed rocky coastline is indicated.

2. Study Area

The Debeli Rtič promontory is located in the north-east part of the Adriatic coast (North Mediterranean Sea), close to the GOT (Figure 1). The study area is in Slovenia, approximately 1 km south of the border with Italy. The surveyed coastline is about 1.2 km-long and incorporates the sea cliff that bounds the promontory of Debeli Rtič (in Italian, Punta Grossa). The latter extends from Lazaret Bay in the north to Koper Bay in the south. The Debeli Rtič promontory is protected as a natural monument, with high amenity value whereby it is frequently visited by locals and tourists throughout the year. The beach at the base of the sea cliff can be reached along the narrow shore platforms from either Lazaret Bay or the tourist village located in the southern part of the promontory. The surveyed coastline has a variable strike, with a trend from the north to the south and counter-clockwise: N90° E, N65° E, N20° E, N310° E, and N290° E (Figure 2). The promontory is characterized by elevations that vary in the range between 10–30 m a.s.l. The sea cliff has variable heights, ranging between a minimum value of 4 m and a maximum value of 18 m. The sea cliff also has a variable dip, ranging from between 50° and 90°, but also includes stretches with some overhanging profiles. In a few high-tilted stretches, the sea cliff is completely devoid of vegetation, whereas in other sectors trees and bushes cover large areas of the slope face. Along the entire coastline, a strip of vegetation covers the extremity of the upper terrace of the promontory continuing up to the cliff crest (Figure 1).

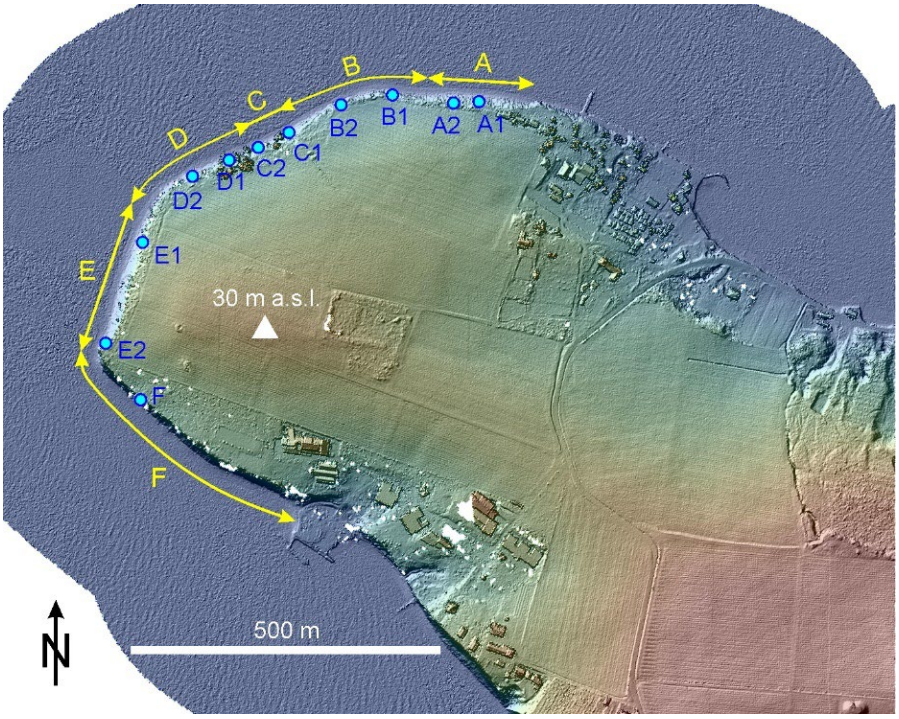

Figure 2. Elevation map of Debeli Rtič obtained from the digital terrain model of the study area (data density: 25 points per m^2). The map also identifies the different sectors forming the sea cliff (yellow stretches A–F) and the location of selected outcrops that are therein included (A1, A2, B1, B2, C1, C2, D1, D2, E1, E2, and F).

From a geological perspective, the study area is characterized by an alternation of marlstones and sandstones of the Flysch of Trieste Formation, which is Eocene in age [21]. The study site is within a larger area characterized by a Dinaric thrust system that includes thrusts, reverse faults, and anticline folds, with a prevailing NW–SE trend [22].

The climate of the study area is Mediterranean (Class C of the Köppen classification, [23]). The meteorological station used for the climatograph (Figure 3a) is located on a pier in Trieste (Italy), 7 km from Debeli Rtič. Mean annual near-surface temperature in

Trieste is approximately 16 °C [24]. On average, the general weather pattern favours sunny days (64.4%), whilst rainy days constitute 31.5%, snowy days 3.0% and hail 1.1% [25]. The hottest month is August (25 °C), whereas winter and autumn are moderately cold, with mean temperatures falling below 10 °C. Annual rainfall is not abundant, yet summers are generally not completely dry. The area is characterized by a prevalence of winds blowing from the first quadrant (Figure 3b), mainly from the ENE (referred to locally as the Bora) [26]. South-easterly winds are important because of a longer geographical fetch (over 800 km). Tides are semi-diurnal, with mean spring-tide values of 0.86 m in Trieste, and mean neap-tide values of 0.22 m [27,28]. The concomitance of spring tides, seiches, south-easterly winds and low atmospheric pressure can cause a sea-level rise of 1.80 m. Mean significant wave height during the year is below 0.5 m [29], while the highest offshore wave height, both for Bora and Scirocco storms, is approximately 5 m [30].

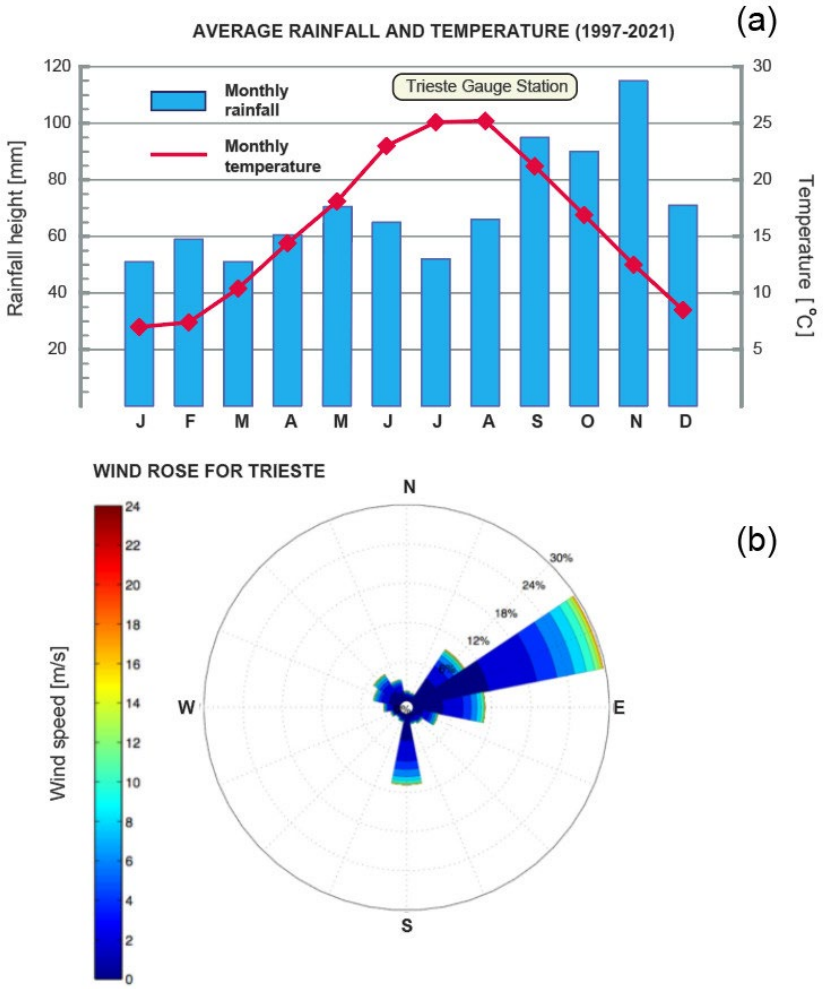

Figure 3. (**a**) Debeli Rtič: climatograph constructed by averaging data recorded since 1997 at the Trieste meteorological station (Molo Bandiera, elev. 1 m a.s.l.); (**b**) Wind rose (Source: [31]).

3. Materials and Methods

The investigations on the sea cliff at Debeli Rtič have been developed by adopting a multidisciplinary approach, which incorporated desk-based activities, field activities (geomechanical survey, GNSS and total station surveys, UAV surveys, collection of MP images) and the use of the DP technique. Preliminary activities focussed on desk-based activities, including the collation of historic aerial images and maps to qualitatively evaluate the extent of cliff retreat at the promontory. Extensive geomechanical field surveys were also carried out with the aim of assessing the rock mass arrangement and identifying rock discontinuity sets in order to later validate the DP-derived outputs. The studied cliff has

been subdivided into six sectors (Sectors A–F in Figure 2) based on the lithological features and structural arrangement of the Flysch rock mass. All sectors forming the sea cliff have been surveyed, and some selected outcrops within them have been investigated in greater detail (Outcrops A1, A2, B1, B2, C1, C2, D1, D2, E1, E2, and F in Figure 2).

Further investigation of the study site was performed via the collection of UAV-images and MP-images. To produce point clouds and 3D models, these images were cocollated and processed using the DP technique. These DP-derived outputs were subsequently used to analyze the rock mass structure that characterizes the steep cliff. These outcomes were eventually compared and validated with the results of the traditional geomechanical survey. The UAV and MP used in this study are relatively inexpensive devices that are widely available. Collectively, with further recent advances in DP software these technologies provide considerable potential for the future investigation of unstable cliffs [32,33]. The workflow, including a simplified schematic diagram of DP procedures that have been applied in this study are shown in Figure 4.

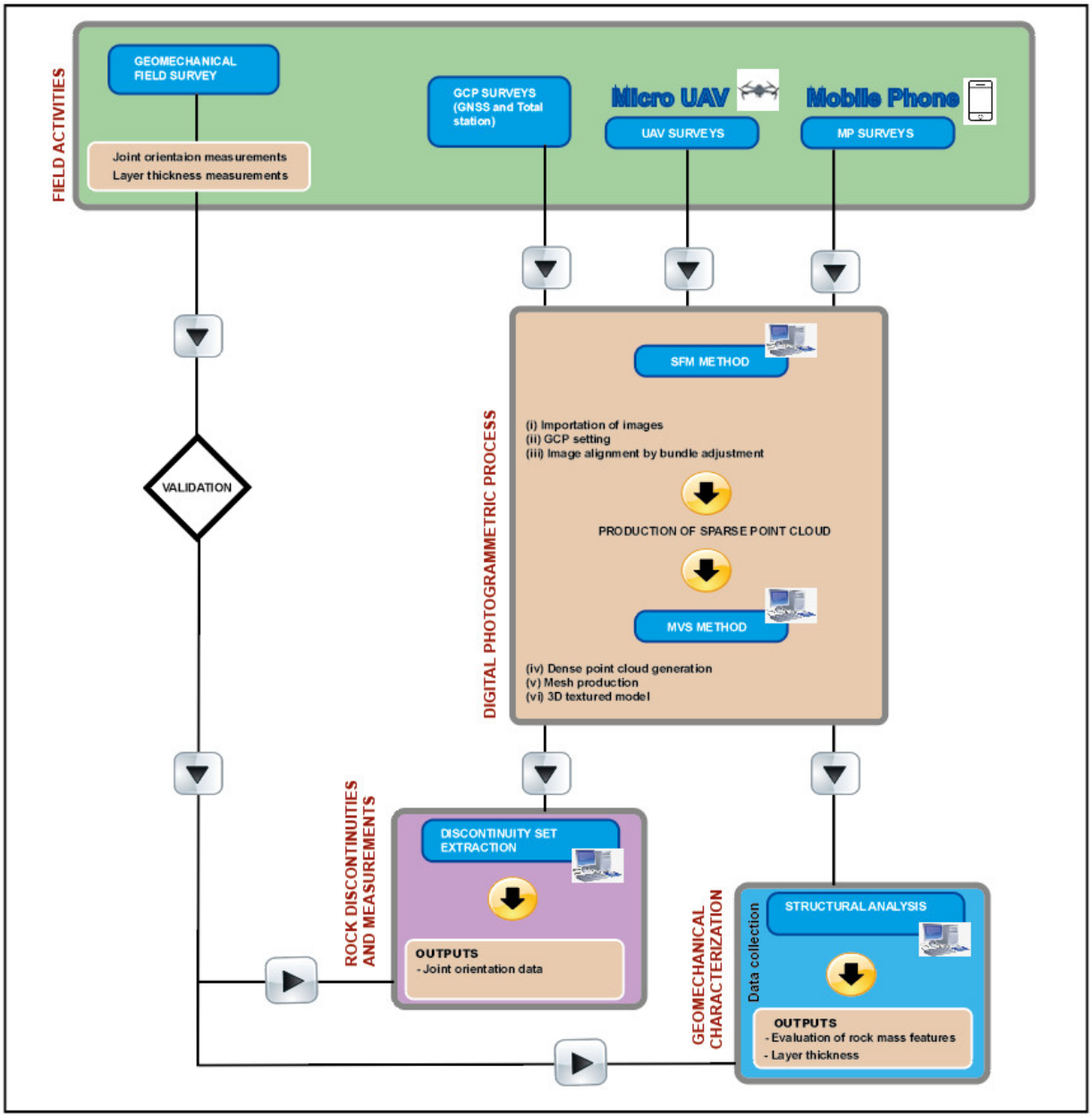

Figure 4. Workflow of the cliff investigation, including photogrammetric procedures.

3.1. Geomechanical Field Survey (Validation)

A traditional geomechanical field survey was performed along the rock cliff at Debeli Rtič in several stages. The main aim of the geomechanical survey was to assess the structural arrangement of the Flysch rock mass, in particular the composition and structure of the rhythmic alternation of sandstone and marl layers, the fracturing pattern of the rock mass and the surface condition of rock discontinuities. A significant amount (N = 105) of orientation data of bedding and fracture joints was collected using a traditional geological compass. However, when considering the height and inclination of the cliff face and the dangerous operating conditions required to survey the rock mass, field measurements were only acquired from a 2 m-high basal strip of the cliff. In addition, a large number of images (many hundreds) were taken during the field surveys. The analysis of these images, repeated at certain time intervals provided key insights to the slope instability processes affecting the sea cliff over time. Field data was acquired from many different outcrops along the surveyed coastline in order to better understand possible variations in the characteristics of the rock mass forming the sea cliff. The detailed examination of key outcrops allowed for the identification of gravity-induced rock mass damage [34], including the presence of newly formed cracking related to the progressive failure mechanism of unstable rock blocks and/or rock masses [35–37].

3.2. GNSS and Total Station Surveys

Ground control points (GCPs) are fixed targets of a known location positioned on the earth's surface. They are used in the processing of DP images to georeference 3D models as well as constrain the photogrammetric bundle adjustment and validate the metric quality of the generated models. To this end, two groups of GCPs were surveyed at Debeli Rtič. The first network of 23 GCPs was distributed along the coast in the form of high contrast squares (size of 0.80 m), which allowed for the precise identification of the central points from both UAV and MP derived images (Figure 5). Three GCPs were set for each surveyed outcrop, in order to georeference the corresponding 3D models.

Figure 5. Spatial distribution of GCPs recorded with GNSS at some specific outcrops along the surveyed rocky coastline.

GCP coordinates were calculated with the Global Navigation Satellite System (GNSS). The measurements were performed using two double-frequency receivers capable of tracking both NAVSTAR and GLONASS constellations in a relative positioning mode. A single reference station was installed on the Debeli Rtič promontory (REF in Figure 5) in order to minimize the distance between the master and rover antennas, enabling the real-time computation of the baselines vector in a local coordinate system. The sampling rate was set at 1 s and the cut-off angle at 15°. The absolute positioning of the reference station in ETRF2000/UTM-F33 coordinate system was calculated by post-processing the phase measurements simultaneously observed at the permanent station of Sgonico (Figure 1), Trieste (TRIE), part of FReDNetwork (Friuli Regional Deformation Network), a geodetic infrastructure of the National Institute of Oceanography and Applied Geophysics (OGS). The absolute accuracy was assessed to be 1–3 cm while the geodetic height of the GCPs was calculated considering the height difference of the TRIE station and by subtracting the constant value of 44.832 m to the ellipsoidic value measured by the GNSS antennas at the test sites; given the short baselines distance (less than 10 km, on average).

A second network of 168 GCPs was surveyed on the cliff face with a Leica TCRA1201 and reflectorless total station from a single station point for each surveyed outcrop. This ensured that each outcrop was evaluated using approximately 20 GCPs. The GCPs correspond with easily identifiable natural targets (mainly rock vertexes) that are distributed on the sub-vertical cliff face and were further used in the DP image processing to constrain and validate the obtained 3D point clouds.

3.3. Image Acquisition–UAV Survey

The UAV survey was carried out in order to obtain information on the rock mass structure particularly in the middle and upper extent of the sea cliff, in areas that were deemed inaccessible and did not allow for the safe collection of geomechanical survey data. Eight UAV surveys were performed in June 2022 using a DJI Spark drone™ (DJI, Nanshan District, Shenzhen, China). This UAV is categorized as a micro drone, according to the weight classification developed by [38]. The widespread proliferation of UAVs has seen them being deployed in various fields of geoscience. They offer major benefits for their low weight, manoeuvrability during flight operations and relatively low cost. These characteristics make it a valuable tool for data acquisition in areas with limited access that are affected by natural geological hazards [33,39–43]. Table 1 lists the main characteristics of the DJI Spark drone™.

Table 1. Main characteristics of the DJI Spark™.

Weight [kg]	Size [mm]	Max Speed [km/h]	Flight Time [min]	Sensor Size [mm]	Effective Focal Length [mm]
0.300	143 × 143 × 55	50	~15	6.17 × 4.56 (3968 × 2976 pixels)	4.4

The DJI Spark drone™ is a vertical take-off and landing (VTOL) quadcopter that can fly for up to 15 min in favourable conditions. The UAV is multi-directional, being able to fly in every direction—horizontally and/or vertically—and can maintain a fixed position. The DJI Spark drone™ is a key component of the unmanned aircraft system (UAS) used for this study. The UAV was piloted without preprogramed flight plans obtaining images every 2 s. Eight UAV surveys were carried out for eight selected outcrops of the cliff (Figure 6 and Table 2). The height of the surveyed stretches of the cliff varied from a minimum value of 6.3 m (outcrop A1) to a maximum value of 17.1 m (outcrop F).

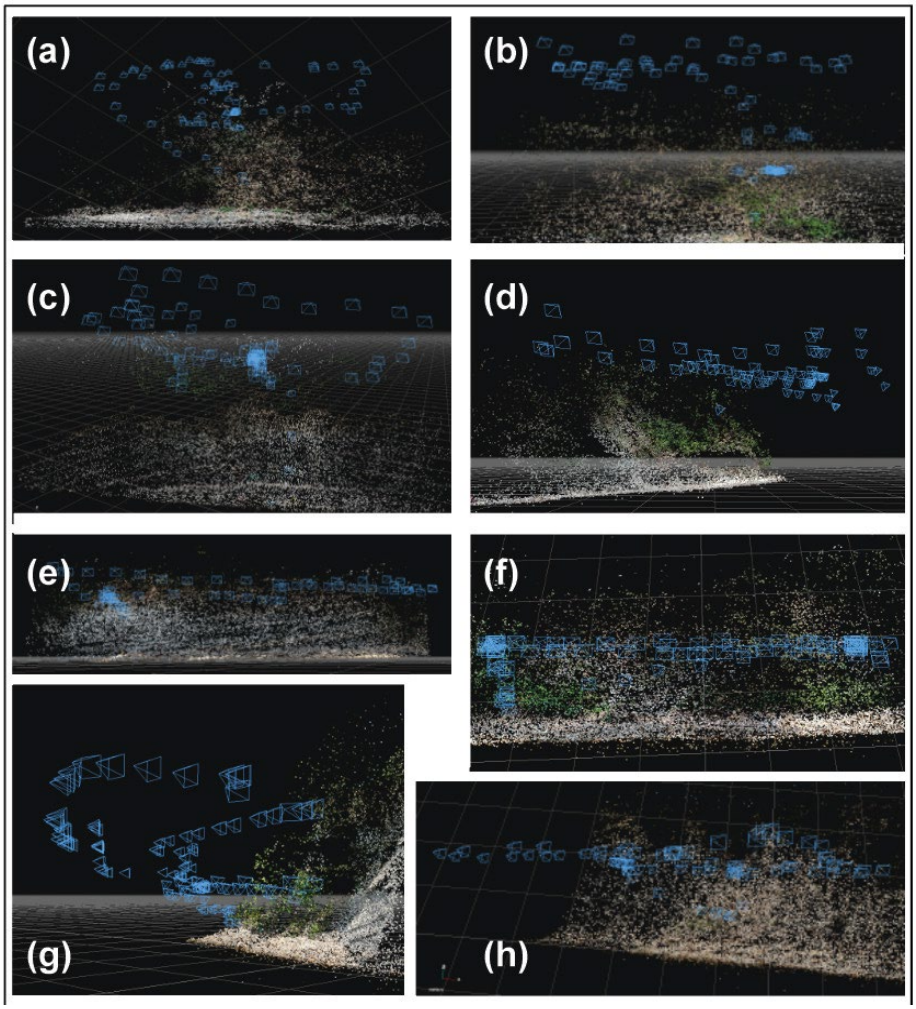

Figure 6. UAV flights showing the positions of the camera (blue framed markers) and the image overlaps of the surveyed outcrops: (**a**) A1, (**b**) A2, (**c**) B2, (**d**) C1, (**e**) D2, (**f**) E1, (**g**) E2, and (**h**) F.

Table 2. Main characteristics of the UAV surveys.

Outcrop	Flight Time [min]	Maximum Flight Height [m]	Number of Pictures	Average Overlap Value [%]	Average Ground Resolution [mm/Pixels]
A1	~3	3.9	86	71.95	3.68
A2	~3	9.0	91	72.43	5.69
B2	~4	11.0	103	71.09	5.19
C1	~3	7.5	80	73.29	6.30
D2	~2	16.6	68	68.97	6.75
E1	~5	7.0	96	79.07	5.28
E2	~4	4.5	104	72.44	3.92
F	~3	9.6	78	74.59	6.47

During the manually operated flight, the UAV maintained a minimum average distance of three meters from the steep cliff face. This distance was chosen due to the presence of dense vegetation and trees occurring along the cliff. Most of the trees are horizontally tilted or partially collapsed, thus creating obstacles for the pilot's activities that hinder the safe deployment of the UAV; hence the decision to undertake manual flight operations. The camera orientation was variably oriented, but was frequently set at approximately 45° towards the terrain in order to avoid reduced coverage of the vertical structure. The

average overlap values vary between 68.97% and 79.07% (Table 2), with maximum overlap values that are in the middle of each scene and exceed 80%. Averaged values of Ground Resolution vary in the range 3.68–6.75 mm/pixels.

3.4. Image Acquisition—Mobile Phone Survey

The MP survey was carried out in order to test the effectiveness of this procedure for the evaluation of the rock mass structure in rock slope stability problems. Six MP surveys were performed at the beginning of June 2022 using an iPhone 12 Pro Max™ (Apple Inc., Cupertino, CA, US). High resolution (HR) images were obtained at various elevations roughly perpendicular to the sea cliff. The iPhone 12 Pro Max™ is equipped with three rear cameras (12MP wide-angle, f/1.6; 12MP ultra-wide-angle, f/2.4; 12MP telephoto, f/2.0) with 2/2.5× optical and 10× digital zoom capacity. Image capture was obtained using the 12MP wide-angle camera. The MP is equipped with a GNSS receiver and comes with built-in support for GPS, GLONASS, Galileo, QZSS and BeiDou satellites systems. The GNSS raw data is not directly accessible and the location information in the iPhone 12 Pro Max™ is provided by the Apple Core Location framework, which combines data provided by all the localization capabilities available on the device, including the Wi-Fi network, GNSS, and Bluetooth. In most mobile phones and tablets, the GNSS signal is continuously updated to achieve progressively accurate locations with errors up to a few tens of cm after many tens of minutes of recording. Conversely, the iPhone 12 Pro Max™ uses a fast stabilization procedure, which is not settable by the user, and provides the local coordinates within only a few tens of seconds [44]. Tavani et al. [44] observed that the accuracy of this model is lower than approximately 10 m. Table 3 lists the main characteristics of the MP adopted. Image acquisition was carried out in automatic mode with parameters reported in Table 3. The WGS84 plan and altimetric coordinate system was used, and the coordinates subsequently corrected with the aforementioned GCPs. The point clouds obtained from MP-DP were used for morphological comparisons with UAV-DP.

Table 3. Main characteristics of the iPhone 12 Pro Max™.

Weight [kg]	Size [mm]	Time of Acquisition [min]	Camera Sensor	Focal Length [mm]
0.226	160.8 × 78.1 × 7.4	~3	1/3.4″	2.2

Image acquisition was conducted with the MP mounted on a 1.7 m-long selfie stick. Images were taken approximately every second using a remote controller. Multiple images were obtained from the seven selected outcrops included within the six sectors of the cliff promontory. (A–F in Figure 2). Table 4 lists the main features of the MP surveys.

Table 4. Main characteristics of MP surveys.

Outcrop	Survey Time [min]	Number of Pictures	Average Overlap Value [%]	Average Ground Resolution [mm/Pixels]
A1	~5	64	72.35	0.646
B2	~6	65	75.47	1.16
C1	~8	116	80.34	0.79
D2	~12	213	73.19	1.09
E2	~10	139	83.33	0.84
F2	~15	96	83.34	0.84

Images were collected from an average distance of one meter from the cliff face. This distance was selected to guarantee a balance between image quality and the number of images taken. The camera orientation was variable in order to provide complete and uniform acquisition of the vertical joints that characterize the cliff.

3.5. Photogrammetric Processing–Point Clouds and 3D Models

A total of 706 UAV-derived images and 693 MP-derived images were processed separately to produce two separate dense point clouds and 3D models for each sector of the cliff, according to the DP technique. The first part of DP is known as Structure from Motion (SfM), which includes three phases: (i) importation of images of each outcrop; (ii) GCP setting; and (iii) image alignment by bundle adjustment.

Images of each outcrop were imported to the Agisoft Metashape (Agisoft LLC, St. Petersburg, Russia), a robust software package widely used with the DP technique. The above-cited software includes SfM algorithms that allow the user to align the images and calculate their relative position to each other (image alignment phase). The outcome of the image alignment process was a sparse point cloud of the investigated cliff and the adjacent shore platform. When constructing the sparse point cloud, the GCPs surveyed with GNSS were used to georeference the point cloud; whereas some of the GCPs surveyed with the total station (at least 10 GCPs for each outcrop) were incorporated in the image processing to avoid long wave deformations of the model, such as cushion or barrel distortions (bundle adjustment).

The second part of DP process is known as Multi-View Stereo (MVS) matching and includes: (iv) dense point cloud production; (v) mesh production; and (vi) generation of a 3D textured model (Figure 4). The low-density point cloud is thickened by increasing the number of points generating a dense point cloud. The dense point cloud was also checked against the remaining GCPs for its metric quality assessment. The final processing steps saw the production of a 3D surface (mesh) and finally, the 3D textured models.

When evaluating the 3D models to extract information on joint orientation data and rock mass arrangement, the dense point clouds were preliminarily cleaned by manually removing all spurious elements without any structural significance (e.g., collapsed blocks, vegetation, trees). In addition, for highly extended outcrops, the dense point clouds were cropped to avoid points that would have weighed the computation down without any further benefit.

3.6. Discontinuity Set Extraction

According to the RS approach, joint orientation data was obtained via semi-automatic extraction from a HR 3D point cloud representing the investigated outcrops [32,45,46]. SfM is widely used to reconstruct a 3D digital model of rock outcrops with the aim of identifying joint sets within the rock mass [47,48]. Following this procedure, the point clouds representing the 3D digital models of some outcrops of the investigated sea cliff at Debeli Rtič were evaluated in order to extract the rock joint sets by using the software Discontinuity Set Extractor (DSE) [49,50]. The DSE is an open-source software that is increasingly used by researchers to identify discontinuity sets affecting rock masses [51]. The methodology adopted in DSE is essentially based on three main steps [52]: (i) a nearest neighbour search aimed at the determination of the plane orientation in each point of the cloud (coplanarity test); (ii) a statistical analysis of the planes, consisting of the determination of their average orientations through a kernel density estimation, identifying those points that belong to the same discontinuity set (semi-automatic set identification); and (iii) a cluster analysis with the localisation of points defining the different clusters and calculation of the plane equations. However, the semi-automatic joint set extraction is strongly sensitive to some controlling parameters embedded in DSE, in particular the *k*-nearest neighbours (*knn*) and the minimum angle between the normal vectors associated with points belonging to different discontinuity sets (*Angle min v ppal*) and requires the control of the user in defining the values of these key parameters [53]. To this aim, the calculated discontinuity orientation data was compared and validated with joint measurements that were directly acquired in the field by using a traditional geological compass. This comparison allowed for the validation of joint set identification and to properly assess the structural arrangement of the rock mass [53].

4. Historical Maps and Images

A detailed map of the San Bartolomeo/Sv. Jernej Bay produced in 1756 by Visconti shows a topographical and geomorphological setting very similar to the present-day form at Debeli Rtič (Figure 7a). Notably, the map also identifies the existence of a votive church at Debeli Rtič which does not appear on subsequent documents and maps. The Italian topographic map from 1916, produced at a 1:25,000 scale (Figure 7b) identifies a seamark exactly 1 mile from the one at Punta Sottile in Italy. These seamarks were used during the nineteenth century to measure the speed of new ships built in the local shipyards. However, the seamark is no longer present on the 1959 sheet of the Italian cartography institute, "Istituto Geografico Militare Italiano" (Figure 7c). Similarly, the seamark is not identifiable on the 1957 (Figure 7d) and 1984 (Figure 7e) aerial images from the Italian Aeronautical Institute.

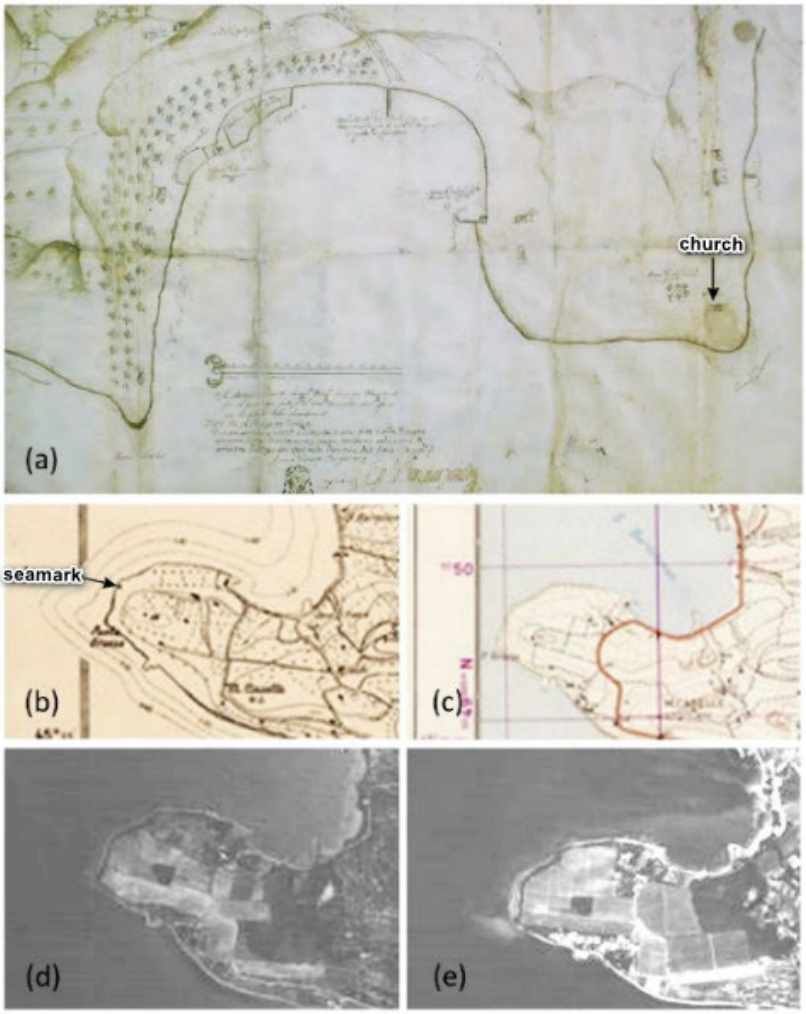

Figure 7. Historical maps and aerial images of Debeli Rtič/Punta Grossa: (**a**) The 1756 Visconti map of the San Bartolomeo Bay with the votive church identified; (**b**) excerpt of the 1916 topographical map at 1:25,000 map of the Italian Military Institute (IGM) with the seamark identified; (**c**) excerpt of the 1959 topographical map at 1:25,000 map of the Italian Military Institute (IGM); (**d**) Debeli Rtič in the 1957 aerial image; (**e**) Debeli Rtič in the 1984 aerial image.

5. Results of Geomechanical Field Survey

The geomechanical survey established that the lithological composition of the Flysch rock mass was not constant along the sea cliff. In some sectors sandstones prevailed over marlstones, whereas in other sectors the opposite occurred. This evidence was later evaluated in a quantitative manner by calculating the sandstone/marl ratio (R) from the 3D digital

models of the surveyed outcrops. In addition, some measurements of the layer thickness of sandstones and marlstones were acquired from different outcrops. The maximum thickness recorded for sandstones was 0.4–0.5 m, whereas the minimum thickness was 0.02–0.03 m. As for the marls, the layer thickness varied between 0.005–0.05 m. However, overlying marl layers reached a maximum thickness of 4–5 m. Conversely, very few adjacent sandstone layers were observed.

A number of joint orientation measurements were acquired from the different rock outcrops. The discontinuity pattern of the rock mass was almost constant over the entire surveyed area, and seven rock joint sets were identified (Figure 8 and Table 5). The sub-horizontal bedding planes (ST) showed an almost constant trend, whereas joint sets J1–J6 included sub-vertical fractures that were all sub-perpendicular to the stratification joints.

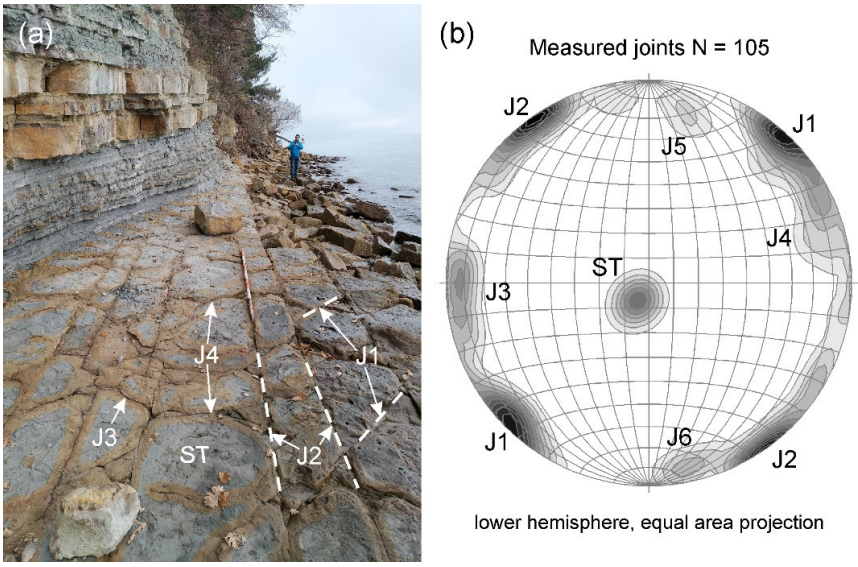

Figure 8. Rock discontinuity sets characterizing the Flysch rock mass at Debeli Rtič: (**a**) main joint sets measured on a thick sandstone layer; and (**b**) contour pole plot of joint orientation measurements.

Table 5. Orientation data of measured joint sets.

Joint Set	Joint Type	Dip Direction [N°E] Mean ± St. Dev.	Dip [°] Mean ± St. Dev.
ST	bedding	032 ± 07	09 ± 07
J1	fracture	044 ± 10	90 ± 05
J2	fracture	145 ± 11	88 ± 05
J3	fracture	089 ± 07	87 ± 04
J4	fracture	248 ± 09	85 ± 08
J5	fracture	192 ± 03	75 ± 04
J6	fracture	348 ± 04	86 ± 04

Field evidence also demonstrated that the surface conditions of rock discontinuities were highly variable. In some cases, joint surfaces were rough and slightly weathered and/or oxidized, whereas in other circumstances the rock surfaces were highly oxidized. Several encrustations of calcite were identified over large areas of the cliff. Localized water outflows were identified along the cliff, even during dry periods. The widespread and combined presence of water outflows and calcite encrustations testifies to a considerable freshwater circulation within the interconnected and open joint system of the rock mass.

6. Results of Photogrammetric Procedures

6.1. UAV-DP Products

The outcomes of UAV-DP are shown in Figure 9 and summarized in Table 6. The UAV-derived 3D models were later evaluated to obtain quantitative information on the structure of the rhythmic alternation of sandstone and marl layers of the Flysch rock mass, particularly in the inaccessible middle–upper part of the cliff. To this aim, in the post-processing stage, the UAV-derived dense point clouds required a manual and time-consuming cleaning exercise to remove vegetation, thus eliminating points without any geological context. Outcomes of the analysis are shown in Figure 9 and discussed in Section 6.3.

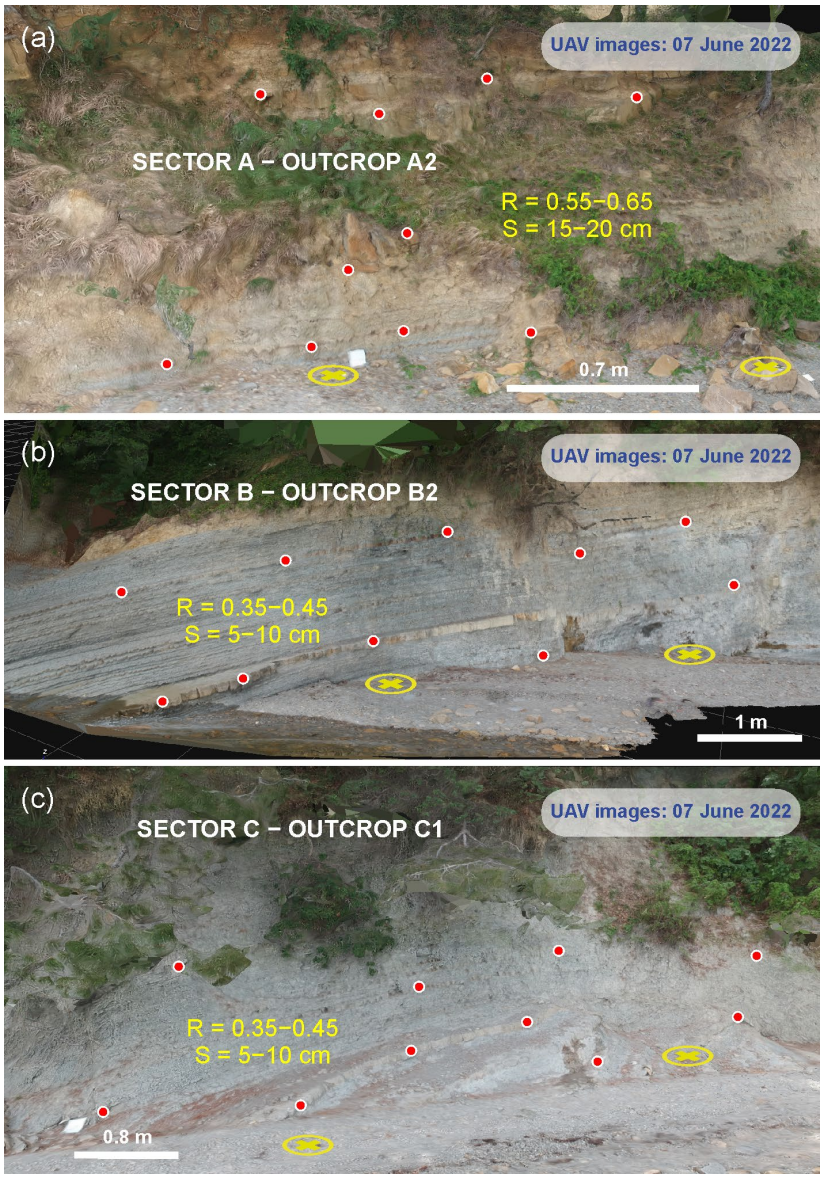

Figure 9. *Cont.*

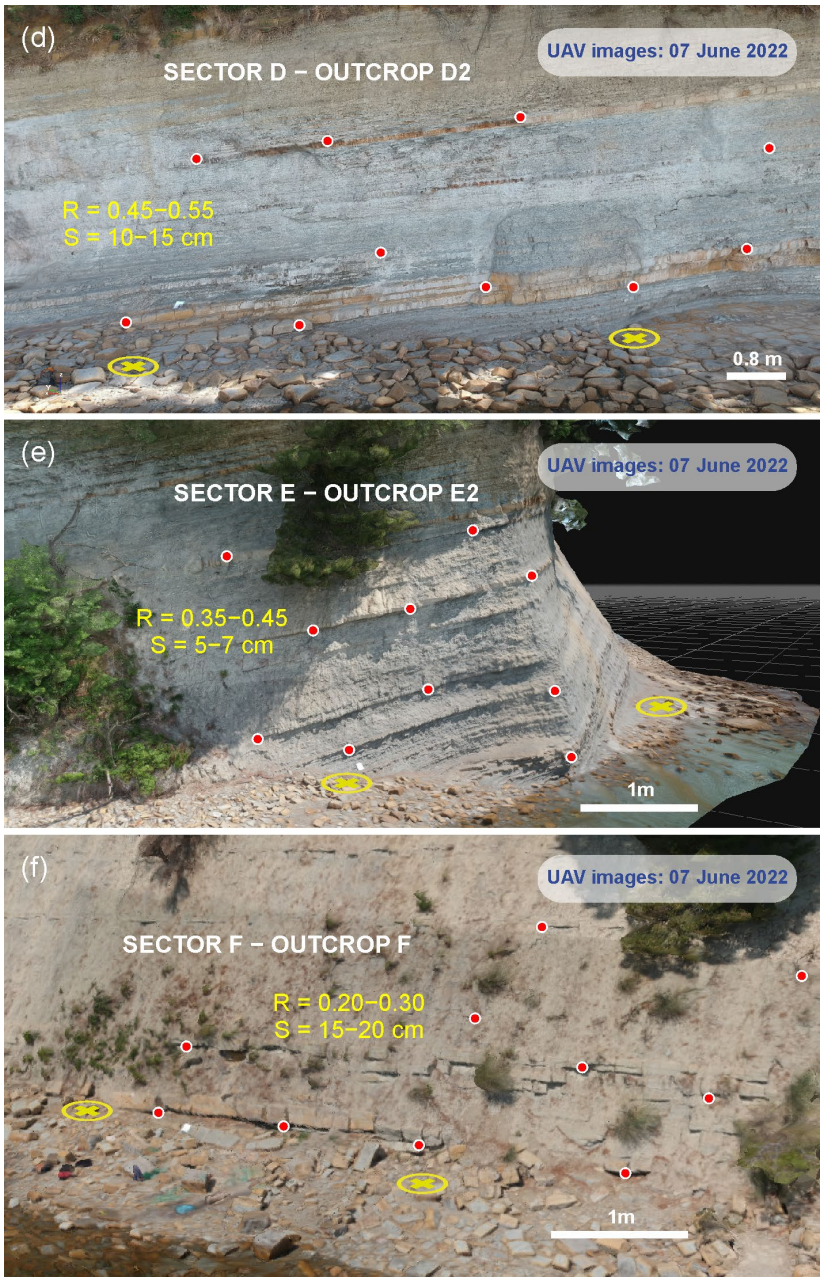

Figure 9. (**a**–**f**). 3D surface models (UAV images) of three sectors along the Flysch Sea cliff at Debeli Rtič. The location of the GCPs used for the point cloud georeferencing (yellow encircled crosses) and for the photogrammetric bundle adjustment (red dots) are shown. Numerical values represent the sandstone/marl ratio (R) and the average thickness of the sandstone layers (S).

Table 6. Number of points forming the clouds and 3D models reconstructed using UAV images.

Outcrop	Sparse Point Cloud	Dense Point Cloud	3D Model Faces
A1	18,688	1,667,902	849,333
A2	18,913	1,639,766	699,800
B2	15,328	1,338,762	651,435
C1	18,036	1,212,275	595,451
D2	20,940	1,207,887	673,105
E1	22,170	1,388,306	769,860
E2	27,298	1,984,823	985,839
F	25,960	1,582,754	767,111

6.2. MP Morphometric Analysis

In total, 693 images were collected from six outcrops at Debeli Rtič, as shown in Table 4. These data were used to build 3D models of outcrops A1, B2, C1, D2, E2 and F (Figure 10 and Table 7).

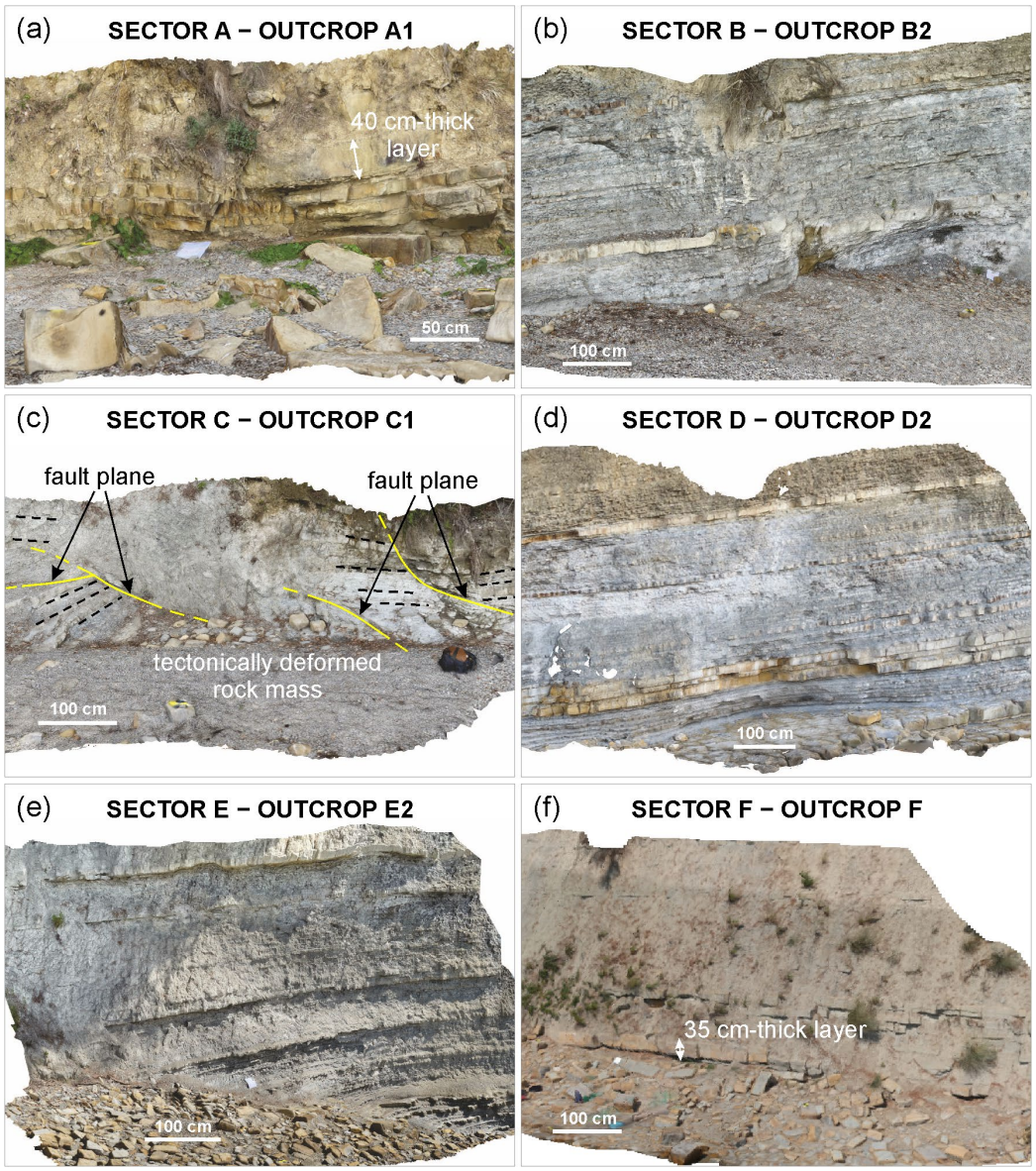

Figure 10. (**a**–**f**). 3D surface models (obtained from MP images) of selected outcrops from the six sectors forming the Flysch Sea cliff at Debeli Rtič.

Table 7. Number of points forming the clouds and 3D models reconstructed using MP images.

Outcrop	Sparse Point Cloud	Dense Point Cloud	3D Model Faces	Maximum Height [m]	Maximum Width [m]
A1	77,514	2,542,852	155,223	3.67	6.06
B2	80,307	2,517,380	134,762	6.95	17.3
C1	149,604	4,675,696	231,890	5.89	18.8
D2	202,577	4,979,530	335,951	9.94	32.6
E2	159,419	5,010,971	315,144	11.1	38.2
F	12,748	683,949	29,564	3.26	5.98

Particular attention was devoted to the 3D digital reconstruction using MP images in order to evaluate the model's reliability compared with the actual morphology and structure of both the shoreline and the cliff face. For this reason, the MP-derived models were assessed focussing mainly on the area at the base of the cliff, which was also investigated with the traditional geomechanical survey. Notably, the MP-derived 3D model representations were consistent with the field evidence. Model A1 in Sector A (Figure 10a) was constructed using 64 images. It covers an area of 6.2 m in length and 2.22 m in height. A pebble beach is present at the cliff toe and in places several detached blocks larger than 0.5 m can be found on the foreshore. Sandstone layers, 0.4 m thick, occur at the base of the cliff, while the collected cliff debris covers underlying bed layers. Model B2 (Figure 10b) in Sector B was constructed using 161 images. It covers an area of 11.3 m in length and 5.3 m in height. A pebble beach occurs at the cliff toe. Centimetre-thick sandstone layers prevail, with a maximum thickness of 0.1 m. Model C1 in Sector C (Figure 10c) was constructed using 116 images. It covers an area of 7.6 m in length and 4.1 m in height. A pebble beach also occurs; however, the cliff toe is characterised by the accumulation of collapsed sandstone blocks. Model D2 in Sector D (Figure 10d) was constructed using 213 images. It covers an area of 14.1 m in length and 7.9 m in height. Centimetre-thick sandstone layers prevail, but some layers up to 0.4 m thick are also present. At the cliff toe, some layers form a sub-horizontal platform partially covered by detached blocks up to 0.5 m in size. Model E2 in Sector E (Figure 10e) was constructed using 139 images. It covers an area of 14.5 m long and 9.2 m in height. Centimetre- to decimetre-thick sandstone layers occur with the deposition of detached blocks up to 0.4 m in size at the cliff toe. Model F in Sector F (Figure 10f) was constructed using 96 images. It covers an area of 5.0 m long and 2.5 m in height. The thickest sandstone layer was found at the base of the cliff (0.35 m thick), while towards the top of the cliff the layers become thinner with the deposition of larger detached blocks at the cliff toe.

6.3. Rock Mass Characterization

The compilation of the UAV-derived 3D surface models of the sea cliff allowed for the evaluation of the sandstone/marl ratio (R) and the determination of the average thickness of sandstone layers (S) within the Flysch sequence for each identified sector (Figure 9). According to data extracted from the point clouds, Sectors A and D were characterized by a slightly higher sandstone/marl ratio (0.45–0.65) compared with the other sectors. These sectors included the thickest sandstone layers outcropping on the sea cliff (0.3–0.5 m). Sectors B and C were characterized by a closely stratified sequence of a prevailing marl content (sandstone/marl ratio = 0.35–0.45). The rock mass included in Sector B was undeformed and homogeneously stratified, whereas the rock mass belonging to Sectors C was highly tectonized, including a number of small folds, evenly truncated, and several faults with a prevailing NW–SE trend (Figure 9). Sectors E and F were made up of a prevailing marly Flysch with a ratio = 0.35–0.45 and 0.20–0.30, respectively. However, Sector E was characterized by a closely stratified sequence with 0.05–0.07 m-thick sandstone layers; whereas Sector F included a few thicker sandstone layers (0.3–0.4 m).

By integrating field evidence on surface conditions of discontinuities and lithological data from the RS-derived 3D point clouds, the Geological Strength Index (GSI) of the Flysch rock masses forming the sea cliff were assessed. This was achieved in accordance with the field characterization originally proposed by [54] (Figure 11). This rock mass characterization is the most widely used classification system for heterogeneous rock masses such as Flysch, and has been reviewed and refined over time, including rating adjustments, to cover a wide range of rock mass types and conditions [55,56]. In this paper, the GSI rating was assigned according to the most recent edition by [56]. The lowest values of GSI were estimated for Sector C, where the Flysch rock mass was highly tectonized (GSI = 30–35). All the other sectors of the sea cliff have higher GSI values, which range between 40 and 55 (Figure 11). Thus, despite the differences detected in-situ on the

lithological composition and discontinuity conditions of the various rock masses, the GSI values vary within a limited range.

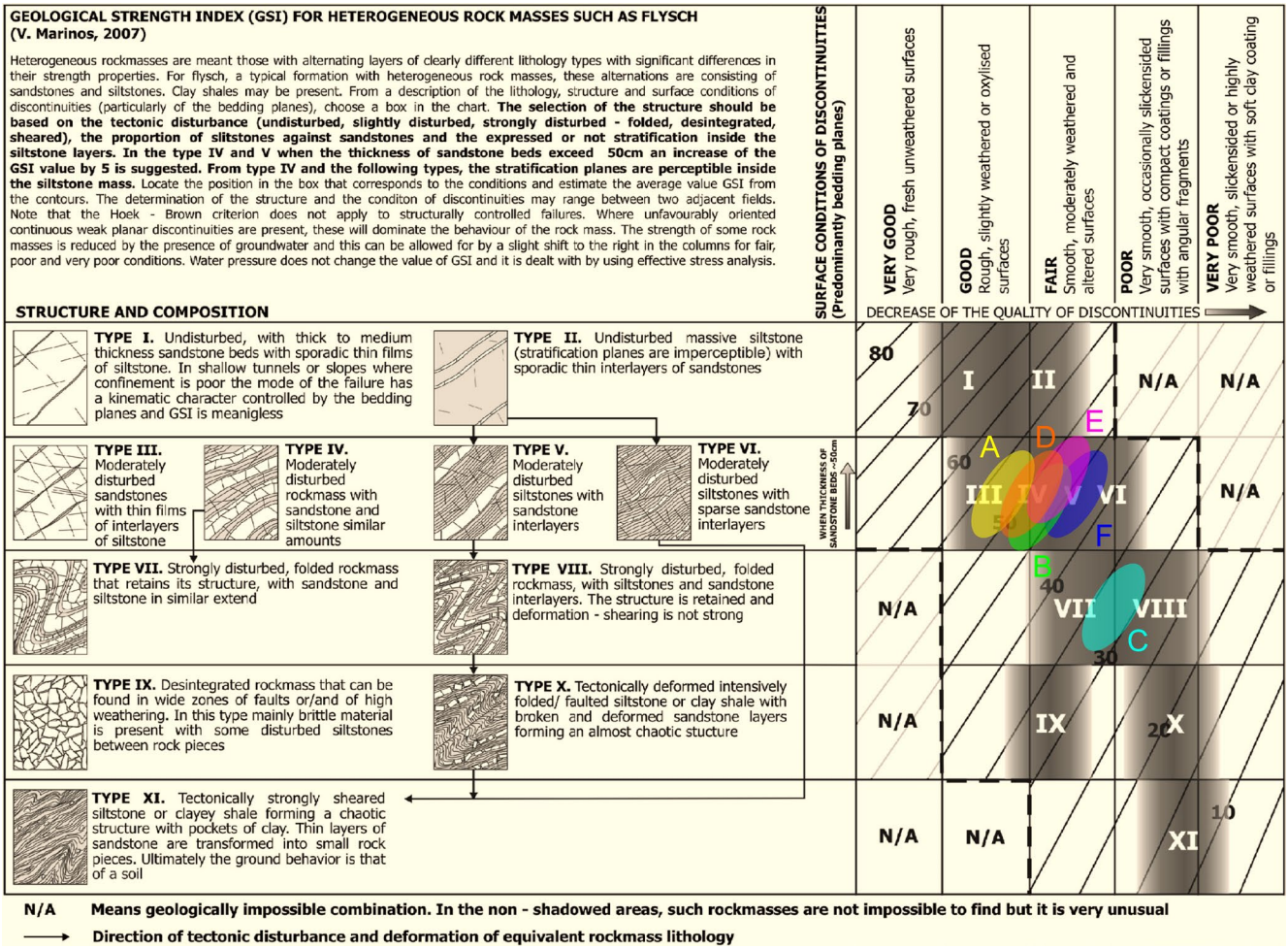

Figure 11. Chart of the Geological Strength Index (GSI) of the various Flysch rock masses characterizing the different sectors of the sea cliff at Debeli Rtič, modified from the original classification of [54] and the last rating assignment of [56].

The MP-derived 3D surface models of the surveyed outcrops of the sea cliff (Figure 10) were elaborated in order to extract the joint set orientation data. However, the semi-automatic joint extraction required a validation with joint orientation measurements that were collected from the field using a traditional geological compass (Figure 8). The joint set extraction was observed to be sensitive to the *knn* and *Angle min v ppal* parameters and required a best-fitting procedure. Figure 12 shows three different joint set extractions that assumed different values of *knn* and *Angle min v ppal* (*Amin*). For *knn* = 20, *Angle min v ppal* = 20 (Figure 12a) and *knn* = 10, *Angle min v ppal* = 10 (Figure 12b), the extracted joint pattern highlighted several differences compared with the measured joint sets (Figure 12d), since some sets were not detected, namely the stratification joints (ST). Conversely, for *knn* = 5, *Angle min v ppal* = 20 (Figure 12c), the extracted joint pattern was consistent with field measurements, despite clear differences in the pattern of the isolines of relative frequency and in the average attitude of the joint sets (Table 8). Some sets were not clearly highlighted by the isolines of relative frequency (in particular, joint sets J2 and J5); whereas joint set J6 was not detected with the semi-automatic extraction. For some discontinuity sets, the calculated dip direction was opposite (i.e., $\pm 180^{\circ}$) to the dip direction

that was measured in the field (Table 8). This difference is due to minor variations in the dip of sub-horizontal and sub-vertical joints (joint sets ST, and J1, J3 and J4, respectively).

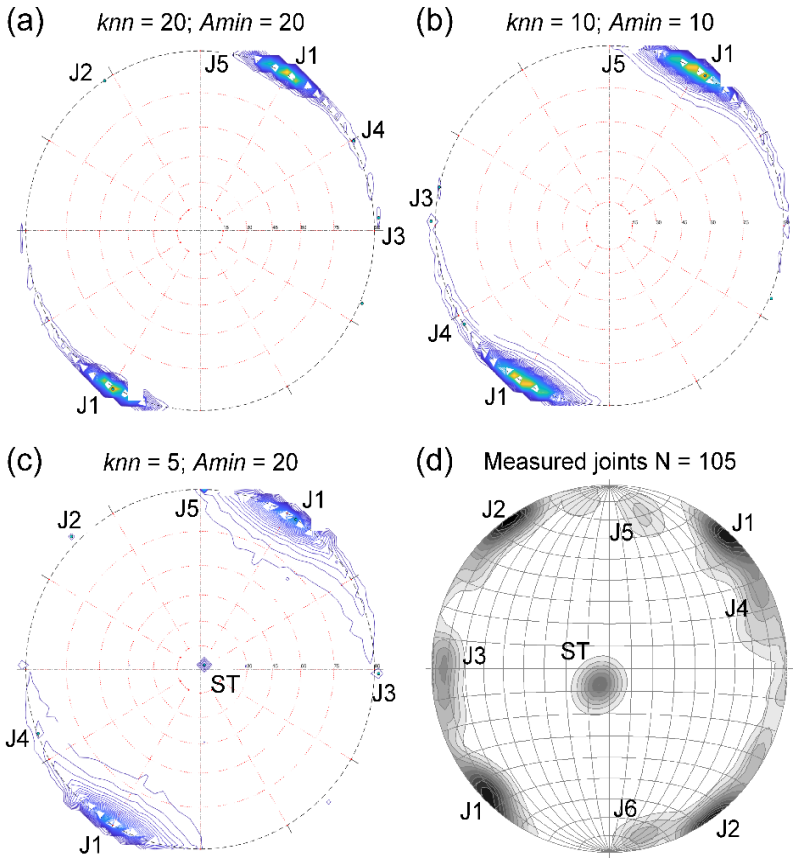

Figure 12. Pole plots of extracted joint sets for different values of the controlling parameters embedded in DSE: (**a**) *knn* = 20 and *Angle min v ppal* = 20; (**b**) *knn* = 10 and *Angle min v ppal* = 10; (**c**) *knn* = 5 and *Angle min v ppal* = 20. (**d**) Stereoplot of joint orientation measurements acquired with the traditional geological compass.

Table 8. Average orientation data of extracted and measured discontinuity sets.

Joint Set	Extracted Joints Dip Direction/Dip [°/°]	Measured Joints Dip Direction/Dip [°/°]
ST	225/04	032/09
J1	213/90	044/90
J2	135/90	145/88
J3	271/90	089/87
J4	069/90	248/85
J5	181/90	192/75
J6	Not detected	348/86

7. Discussion

7.1. Photogrammetric Procedures

In the literature, the UAV-DP approach has successfully been used to study sea cliff instabilities e.g., [57–59]. This method represents a flexible approach in the investigation of slope failures in coastal areas. However, where sea cliffs are covered by vegetation, the manipulation of point clouds becomes more complex. It has largely been proven that vegetation cover on topographic surfaces surveyed using RS techniques often results in incoherent, and inaccurate representations of the actual slope morphology [60–62]. The

presence of vegetation requires manual cleaning of the point cloud in the post-processing stage, which can be time-consuming and results in the creation of voids in the 3D model surface. At Debeli Rtič, UAV-derived point clouds of the sea cliff were strongly affected by dense vegetation cover that significantly masked the underlying rock masses (Figure 13a). It must also be noted that, as this work demonstrates, the presence of vegetation on a cliff face may require manual UAV flights, avoiding the limitations of preprogramed flight plans.

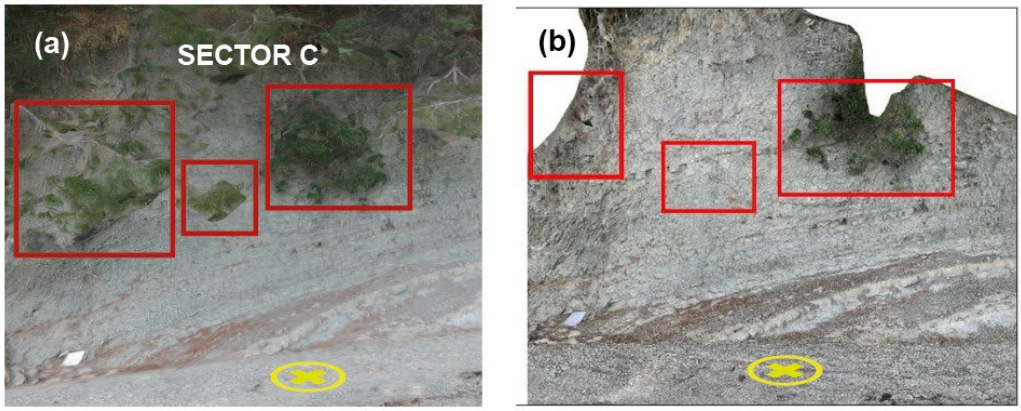

Figure 13. Comparison of photogrammetric models of a sea cliff stretch covered by vegetation: (**a**) 3D model obtained by UAV-derived data; (**b**) 3D model obtained by MP-derived data. Note the differences in the same areas of the outcrop (red squares). The location of the GCPs (yellow encircled crosses) is also shown.

The recent and widespread availability of smartphones with HR cameras, such as the last generation of iPhone devices, allows the user to collect images in close proximity to the cliff [63]. This limits the shadowing effects produced by trees and/or other vegetation which in some circumstances may hinder data acquisition by UAV. The iPhone 12 Pro Max^{TM} has recently been tested to construct dense point clouds in several geoscience studies [44]. The tests carried out at Debeli Rtič using the iPhone 12 Pro Max^{TM} were aimed at evaluating the suitability of the aforementioned MP device to build dense point clouds to help identify rock mass features on a Flysch Sea cliff through validation using UAV-derived data and field surveys. The Lidar functionality of iPhone device was not tested because Tavani et al. [44] noted that the specifications and performance of the iPhone Lidar sensor is significantly lower than survey-grade Lidar tools in terms of resolution (i.e., points per square meter) and noise characteristics.

By processing images captured from the iPhone device it was possible to build dense point clouds and identify the main joint sets and some lithological features of the Flysch rock mass. It was also beneficial in terms of overcoming issues relating to shadowing effects as image acquisition was possible, to some extent, beneath extensive vegetation (Figure 13b). The comparison of the two photogrammetric techniques adopted demonstrates that MP-derived models allow for the removal of vegetation (see the red squares in Figure 13), as images are collected very close to the sea cliff from many orientations with respect to the slope face. This also results in advantages when compared with UAV surveys, which relate to greater ease in collecting a large number of images and a shorter time period to create point clouds in the post-processing stage.

Field surveys permitted to validate the analysis of dense point clouds in recognizing the rock mass arrangement. Notably, field geomechanical investigations confirmed that the Flysch rock mass forming the sea cliff has variable features in its structure, including lithological composition and surface conditions of discontinuities along the whole surveyed coastline. The collated data identifies that MP-derived point clouds can be effective in the evaluation of the rock mass arrangement of sea cliffs.

7.2. Sea Cliff Instability Processes

The detailed analysis of the extensive photographic documentation taken over a 20-year period (both aerial and terrestrial images) [8] allowed for the investigation of the morphological evolution of the Flysch Sea cliff at Debeli Rtič over time. The analysis of these morphological changes helps define the factors driving sea cliff retreat and evolution, including the role played by marine erosion and gravitational slope processes. Field evidence demonstrated that morphological changes affected both the shore platform and the rock cliff. Some selected images are presented in Figure 14. The analysis of these images shows that at the top of the cliff, at the border between Sectors E and F, shallow collapses of marlstones occurred almost continuously, as highlighted by the stripping of a tree root between 2003 and 2014. Moreover, sea cliff instability in Sectors D and F is highlighted by localized slope failures, as indicated by the accumulation of material at the cliff toe (Figure 14). In Sector F, the collapse of a group of trees occurred in 2009.

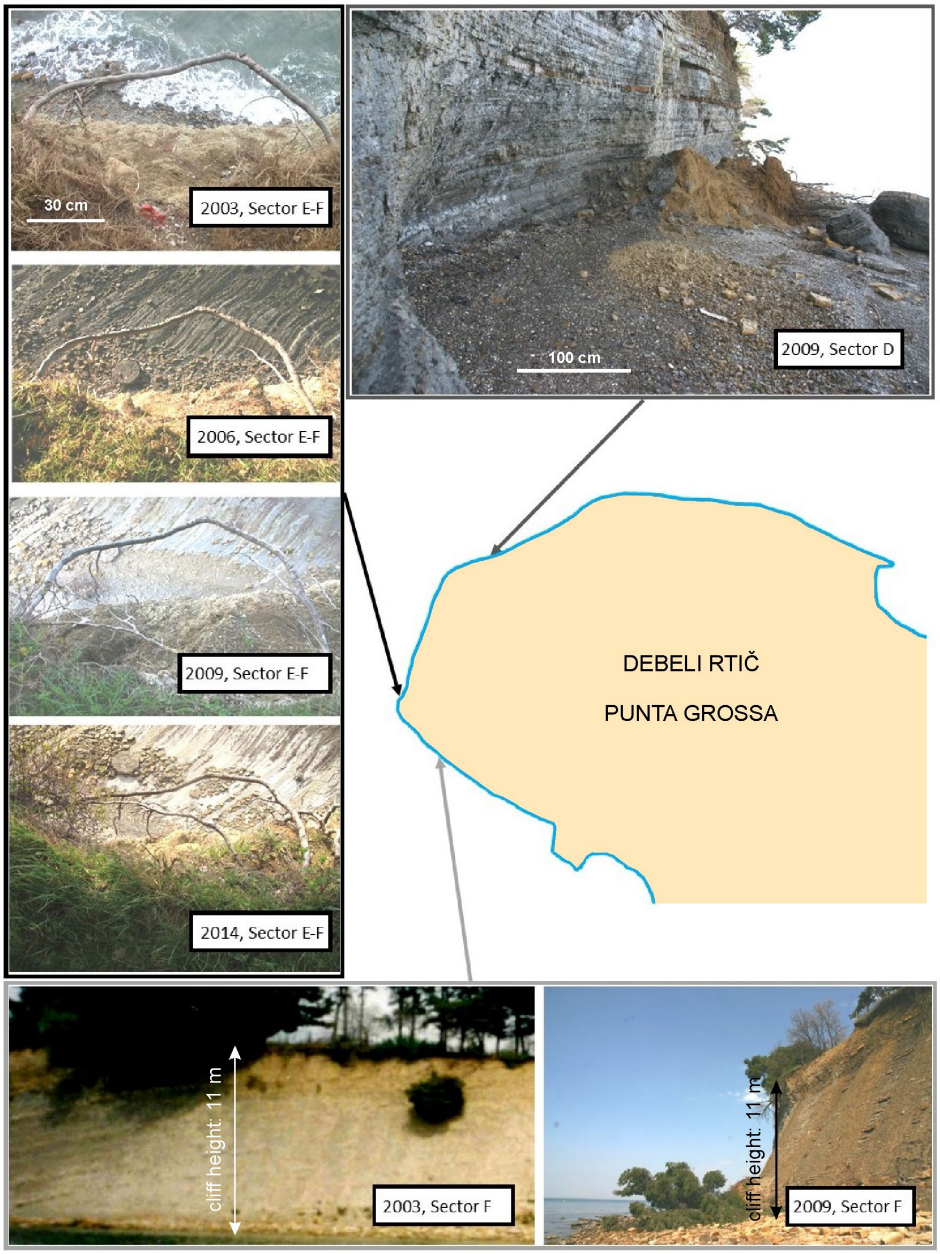

Figure 14. Selected images collected between 2003 and 2014 at the promontory of Debeli Rtič/Punta Grossa. Sea cliff retreat processes are highlighted by slope failures that occurred during the studied period.

The first surveys of the coastline that were carried out during the period 2000–2010 proved the widespread presence of cobbles and pebbles along most of the shore platform (Figure 15a). At various locations along the coast, sandstone blocks and/or small rockfall deposits were also identified. The presence of collapsed trees within the landslide deposits that accumulated on the shore platform demonstrate that rockfalls occurred predominantly from the clifftop where such vegetation is present (Figure 15a).

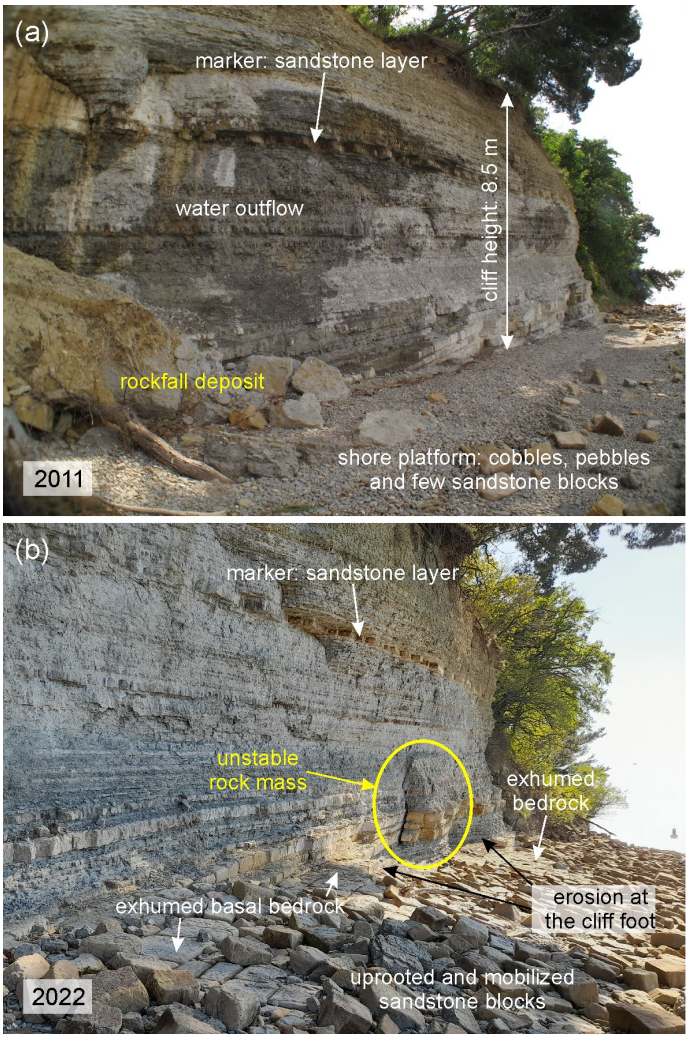

Figure 15. Stretch of the Flysch Sea cliff at Debeli Rtič (Sector D) as photographed in (**a**) 2011 and (**b**) 2022. Note the morphological evolution of the shore platform and the cliff foot caused by the combined action of marine erosion and slope instability processes.

After a few years and at several locations along the coast, cobbles, pebbles, and landslide deposits were almost completely removed from the shore platform, causing the exhumation of the underlying bedrock, which mainly coincides with the thickest sandstone layers (0.2–0.3 m) included in the Flysch sequence (Figure 15b). In addition, a large number of sandstone blocks forming the exhumed bedrock were uprooted and mobilized along the shore platform. The uprooting of the basal bedrock occurred along a number of continuous and mutually intersecting joint sets that internally subdivided the sandstone layers (Figure 8a). As a result of the removal of the debris material and the subsequent exhumation of the underlying bedrock, the shore platform experienced a substantial deepening (0.2–0.4 m, on average), causing the outcropping of some basal layers at the adjacent cliff foot. In some circumstances, the marl layers at the base of the Flysch Sea

cliff were slightly eroded, thus presenting irregular profiles of the slope face, with several overhangs of overlying sandstone layers included in the Flysch sequence (Figure 15b).

According to field evidence, the rock cliff at Debeli Rtič was involved in various slope failures that occurred in the past and is currently affected by a number of unstable blocks and/or rock masses susceptible to failure. These instability phenomena are characterized by different materials, failure mechanisms, kinematics, and volumes. Four different landslide types were recognized (Figure 16):

1. Fall and/or toppling of individual overhanging sandstone slabs (Figure 16a);
2. Sliding and/or toppling of shallow stratified rock masses (Figure 16b);
3. Sliding of larger and deeper rock masses of a prevailing arenaceous Flysch (Figure 16c);
4. Sliding of thin slices of the cliff made up of a prevailing marly Flysch (Figure 16d).

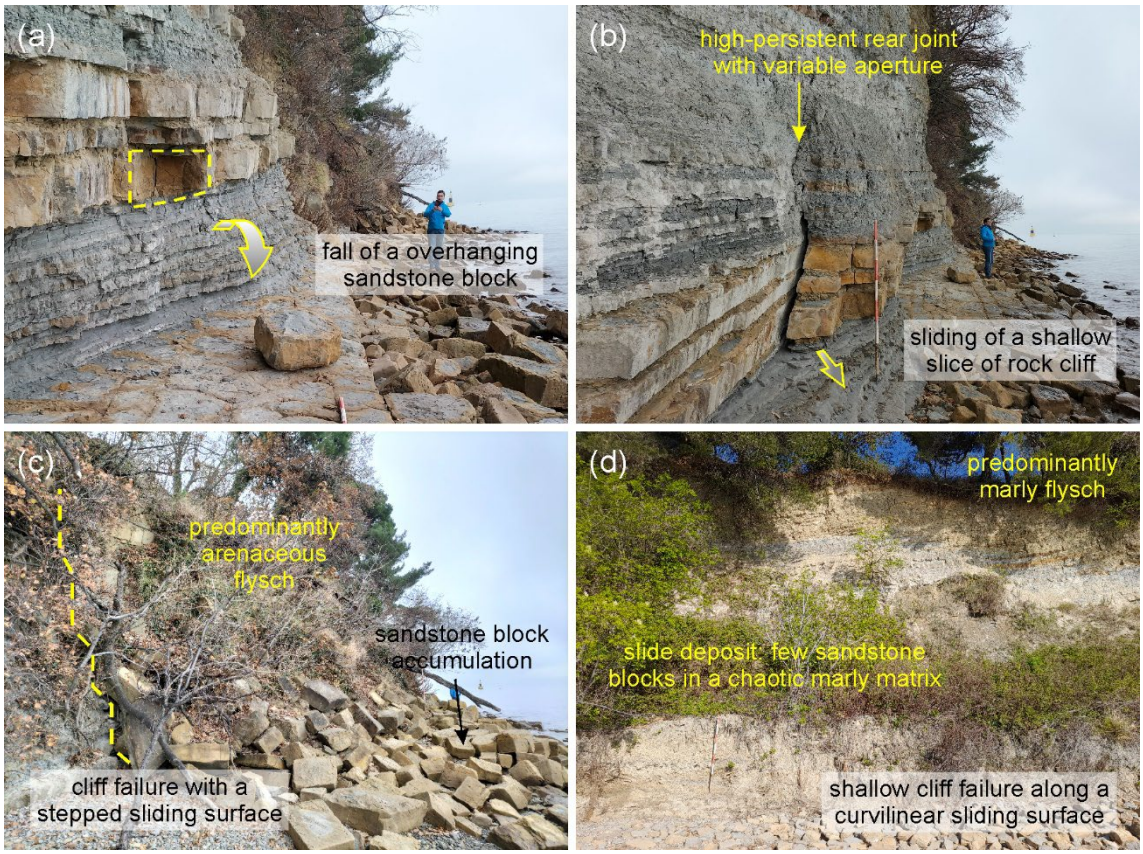

Figure 16. Slope failure types identified along the sea cliff at Debeli Rtič: (**a**) fall/toppling failure of overhanging sandstone blocks; (**b**) sliding/toppling failure of shallow stratified rock masses; (**c**) stepped sliding failure in a predominantly arenaceous Flysch; and (**d**) shallow curvilinear sliding failure in a predominantly marly Flysch.

Most slope failures that occurred in the past were recognized on the basis of the identification of the failed rock mass that accumulated on the basal shore platform and of the source area or detachment surface on the cliff. Unstable rock masses that are currently susceptible to failure were identified on the basis of abundant geomechanical factors relating to: newly formed fractures, zones of intense intact rock cracking, joint opening, internal sliding surfaces and differential block movements.

On the whole, all data presented herein demonstrates that the Debeli Rtič sea cliff is affected by inherent and cumulative, progressive retreat, as evidenced by historical maps (Figure 7) and, more distinctly, by several images that were repeatedly taken over the last 20 years (Figures 14 and 15). Moreover, as also reported by [7,8], sea cliff retreat mainly consists of a dynamic process characterized by local episodic falls, topples and

slides (Figure 16). This study helps in defining the instability processes that affect the sea cliff at Debeli Rtič and the role played by marine erosion and mass-wasting processes in the progressive landward retreat of the cliff. The erosive process performed by sea waves caused a deepening of the shore platform, which in turn caused the outcropping of some weak layers at the cliff foot. As a result, marine erosion is responsible for falls/toppling of some overhanging blocks as well as sliding/toppling of shallow stratified rock masses at the cliff foot (that is, in the lowest 1–2 m of the sea cliff). However, most of the slope failures that were identified along the cliff were caused by slope gravitational processes, which are strongly related to a progressive failure mechanism of unstable rock masses due to weathering processes and progressive fracturing that is mainly caused by freshwater circulation within the jointed rock mass.

The map in Figure 17 shows the location of the identified slope failure types, the distribution of which is related to specific geomechanical factors, including the lithological composition of the rock mass (i.e., the GSI) of the different sectors forming the Flysch Sea cliff. However, it must be noted that some stretches of the cliff were not, and do not currently present any slope failure phenomenon (Figure 17). For instance, no slope failure occurred in Sector C, which is characterized by a rock mass with the lowest values of GSI due to its tectonic disturbance. This has to be taken into account when estimating the strength parameters of the rock masses and further evaluating the slope stability condition (i.e., the factor of safety) of the cliff.

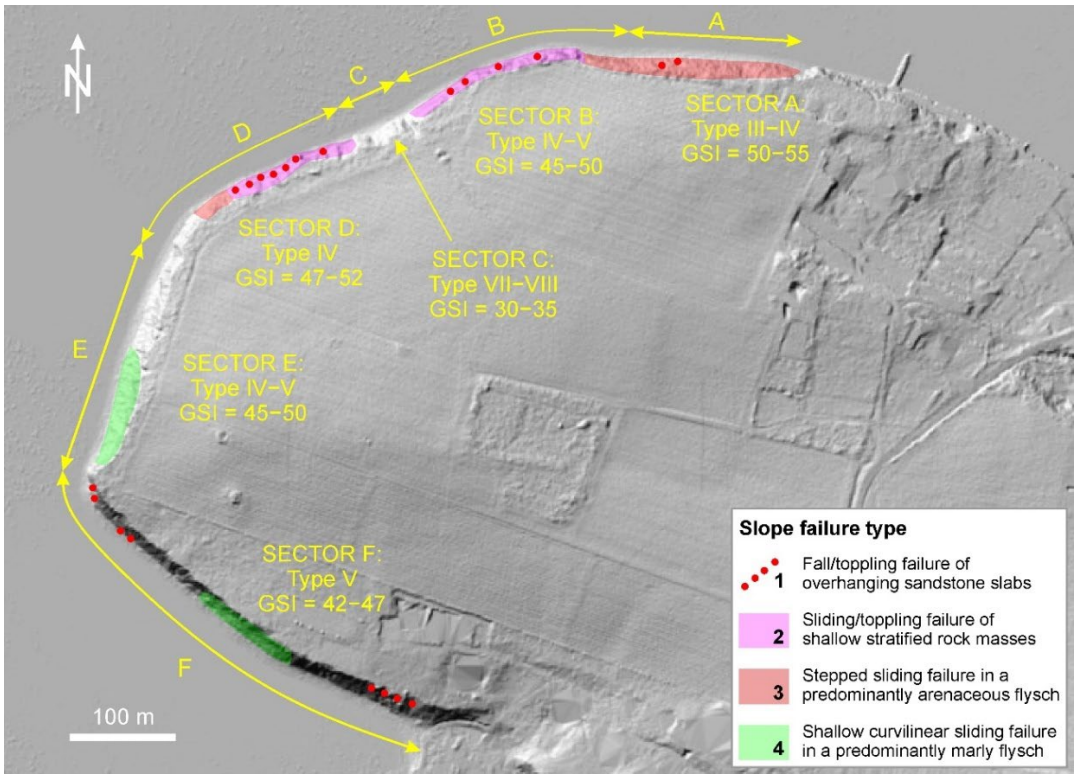

Figure 17. Map of instability phenomena occurring at Debeli Rtič showing the different slope failure types (1–4) involving various sectors (**A**–**F**) of the Flysch Sea cliff.

8. Conclusions

Regarding the study of Debeli Rtič, the identification of the instability processes affecting the sea cliff was possible via the integration of the data acquired from: (i) aerial images; (ii) terrestrial images; (iii) 3D digital model representations, and (iv) geomechanical investigations. The morphological changes that occurred on the shore platform and on the

rock cliff over time were caused by the combined action of marine erosion and gravitational slope processes.

From a methodological viewpoint, this study suggests that:

1. An integrated study approach that combines the results of a geomechanical survey and data obtained using DP is effective in the investigation of slope instability processes affecting a sea cliff. In particular, UAV surveys are useful to obtain information on the rock mass features in inaccessible areas where the traditional geomechanical survey cannot be safely performed;
2. MP devices demonstrate a high degree of suitability for image data acquisition in very particular conditions, such as the presence of partially collapsed horizontal or sub-vertical trees or other vegetation that masks the underlying rock mass;
3. MP-derived point clouds can be effective for the extraction of joint orientation data from steep sea cliffs since images are collected very close to the cliff from many orientations with respect to the slope face;
4. The comparison between UAV-derived products and MP-derived products identified that the use of UAVs allows the user to map large sections of the coast relatively quickly. However, in particular conditions characterized by the presence of vegetation, MP-derived point clouds are easier to manipulate since they do not require extensive cleaning to remove the masking effects of vegetation.

The analyzed case-history demonstrated that basic geological information obtained from the creation of 3D models reconstructed using the RS approach is highly sensitive to both the quality of the dense point clouds and the parameters embedded in the calculation algorithms. In some circumstances, rock mass features were not properly evaluated, thus resulting in unreliable, even erroneous assessments of the rock mass structure. As a result, this paper demonstrates that the use of 3D models obtained from RS techniques has several limitations and always requires the intervention of an expert user and subsequent validation with a significant sample of direct measurements collected from the field, where the study site is accessible.

Future studies of the site will aim to improve the accuracy of the MP-derived dense point clouds through fixed GCPs using steel rods to be installed at the cliff toe. This network will permit the continued monitoring and future modification to the sea cliff over time using MP-DP techniques with extremely high accuracy. The results of future monitoring are also expected to provide valuable insight to the impacts of progressive increases in sea level rise on the instability of sea cliffs.

Author Contributions: Conceptualization, S.F., A.B. and S.D.; GNSS survey, M.M.; UAV survey, S.D.; MP survey, S.F.; geomechanical survey, A.B. and S.D.; software, S.F., A.B. and S.D.; writing review and editing, S.F., A.B., S.D. and L.H.; supervision, S.F., A.B. and S.D. All authors have read and agreed to the published version of the manuscript.

Funding: This research was carried out in the frame of the Project "Landslide Susceptibility Analysis of Rocky Coasts in the North Adriatic Sea (Italy, Slovenia, Croatia)" supported by the University of Trieste, Italy, and the University of Udine, Italy.

Data Availability Statement: The data presented in this study are available on request from the corresponding author.

Acknowledgments: We are grateful to Michele Fernetti (University of Trieste), Pietro Grego, and Andrea Morosetti for their support during field activities.

Conflicts of Interest: The authors declare no conflict of interest. Apple Inc. (Cupertino, California, US) and DJI™ (Nanchan District, Shenzhen, China) had no role in the design of the study; in the collection, analyses, or interpretation of data; in the writing of the paper, or in the decision to publish the results.

Abbreviations

The following abbreviations are used in the manuscript:

DP	Digital Photogrammetry
UAV	Unmanned Aerial Vehicle
MP	Mobile Phone
GOT	Gulf of Trieste
RS	Remote Sensing
SfM	Structure from Motion
MVS	Multi-View Stereo
a.s.l.	above sea level
GCP	Ground Control Point
GNSS	Global Navigation Satellite System
VTOL	Vertical Take Off and Landing
UAS	Unmanned Aerial System
HR	High Resolution
DSE	Discontinuity Set Extractor
GSI	Geological Strength Index

References

1. Kennedy, D.M.; Stephenson, W.J.; Naylor, L.A. Introduction to the rock coasts of the world. *Geol. Soc. Lond. Mem.* **2014**, *40*, 1–5. [CrossRef]
2. Furlani, S.; Pappalardo, M.; Gómez-Pujol, L.; Chelli, A. The rock coast of the Mediterranean and Black Seas. *Geol. Soc. Lond. Mem.* **2014**, *40*, 89–122. [CrossRef]
3. Salman, A.; Lombardo, S.; Doody, P. Living with Coastal Erosion in Europe: Sediment and Space for Sustainability. Eurosion Project Reports. *Off. Off. Publ. Eur. Communities* **2004**. Available online: http://resolver.tudelft.nl/uuid:483327a3-dcf7-4bd0-a986-21d9c8ec274e (accessed on 16 July 2022).
4. Young, A.P. Decadal-scale coastal cliff retreat in southern and central California. *Geomorphology* **2018**, *300*, 164–175. [CrossRef]
5. Young, A.P.; Carilli, J.E. Global distribution of coastal cliffs. *Earth Surf. Process. Landf.* **2019**, *44*, 1309–1316. [CrossRef]
6. Biolchi, S.; Furlani, S.; Covelli, S.; Busetti, M.; Cucchi, F. Morphoneotectonic map of the coastal sector of the Gulf of Trieste (NE Italy). *J. Maps* **2016**, *12*, 936–946. [CrossRef]
7. Furlani, S. Shore platforms along the Northwestern istrian coast: An overview. *Ann. Ser. Hist. Nat.* **2003**, *13*, 247–256.
8. Furlani, S.; Devoto, S.; Biolchi, S.; Cucchi, F. Factors Triggering Sea Cliff Retreat Instability Along the Slovenian Coast. *J. Coast Res.* **2011**, *61*, 387–393. [CrossRef]
9. Paronuzzi, P.; Bolla, A.; Rigo, E. 3D stress-strain analysis of a failed limestone wedge influenced by an intact rock bridge. *Rock Mech. Rock Eng.* **2016**, *49*, 3223–3242. [CrossRef]
10. Gigli, G.; Casagli, N. Semi-automatic extraction of rock mass structural data from high resolution LIDAR point clouds. *Int. J. Rock Mech. Min. Sci.* **2011**, *48*, 187–198. [CrossRef]
11. Sturzenegger, M.; Stead, D.; Elmo, D. Terrestrial remote sensing-based estimation of mean trace length, trace intensity and block size/shape. *Eng. Geol.* **2011**, *119*, 96–111. [CrossRef]
12. Battulwar, R.; Zare Naghadehi, M.; Emami, E.; Sattarvand, J. A state-of-the-art review of automated extraction of rock mass discontinuity characteristics using three-dimensional surface models. *J. Rock Mech. Geotech.* **2021**, *13*, 920–936. [CrossRef]
13. Corradetti, A.; Tavani, S.; Parente, M.; Iannace, A.; Vinci, F.; Pirmez, C.; Torrieri, S.; Giorgioni, M.; Pignalosa, A.; Mazzoli, S. Distribution and arrest of vertical through-going joints in a seismic-scale carbonate platform exposure (Sorrento peninsula, Italy): Insights from integrating field survey and digital outcrop model. *J. Struct. Geol.* **2017**, *108*, 121–136. [CrossRef]
14. Salvini, R.; Mastrorocco, G.; Esposito, G.; Di Bartolo, S.; Coggan, J.; Vanneschi, C. Use of a remotely piloted aircraft system for hazard assessment in a rocky mining area (Lucca, Italy). *Nat. Hazards Earth Syst. Sci.* **2018**, *18*, 287–302. [CrossRef]
15. Donati, D.; Stead, D.; Brideau, M.-A.; Ghirotti, M. Using pre-failure and post-failure remote sensing data to constrain the three-dimensional numerical model of a large rock slope failure. *Landslides* **2021**, *18*, 827–847. [CrossRef]
16. Schilirò, L.; Robiati, C.; Smeraglia, L.; Vinci, F.; Iannace, A.; Parente, M.; Tavani, S. An integrated approach for the reconstruction of rockfall scenarios from UAV and satellite-based data in the Sorrento Peninsula (southern Italy). *Eng. Geol.* **2022**, *308*, 106795. [CrossRef]
17. Stoop, J. New Ways to Use Smartphone for Science. *Elsevier Connect* **2017**. Available online: https://www.elsevier.com/connect/new-ways-to-use-smartphones-for-science (accessed on 26 July 2022).
18. Weng, Y.-H.; Sun, F.-S.; Grigsby, J.D. GeoTools: An android phone application in geology. *Comput. Geosci.* **2012**, *44*, 24–30. [CrossRef]
19. Xie, Y.; Gao, G.; Niu, N.; Wang, Y. Exploration and practice of the use of mobile devices to assist in general geological field practice. *J. Geogr. High. Educ.* **2021**. [CrossRef]
20. Corradetti, A.; Seers, T.D.; Billi, A.; Tavani, S. Virtual outcrops in a pocket: Smartphone as a fully equipped photogrammetric data acquisition tool. *GSA Today* **2021**, *31*, 4–9. [CrossRef]
21. Jurkovšek, B.; Biolchi, S.; Furlani, S.; Jurkovšek, T.; Zini, L.; Jež, J.; Tunis, G.; Bavec, M.; Cucchi, F. Geology of the Classical Karst Region (SW-NE Italy). *J Maps* **2016**, *12*, 352–362. [CrossRef]
22. Placer, L. Strukturne posebnosti severne Istre (Structural curiosity of the northern Istria). *Geologija* **2005**, *48*, 245–251. (In Slovenian) [CrossRef]
23. Köppen, W. *Grundriss der Klimakunde*, 2nd ed.; Walter de Gruyter: Berlin, Germany, 1931.

24. Raicich, F.; Colucci, R.R. A near-surface temperature time series from Trieste, northern Adriatic Sea (1899–2015). *Earth Syst. Sci. Data* **2019**, *11*, 761–768. [CrossRef]
25. Tommasini, T. Dieci anni di osservazioni meteorologiche a Borgo Grotta Gigante sul Carso Triestino (1967–1976). *Atti Mem. Della Comm. Grotte E. Boegan* **1979**, *24*, 1–11.
26. Carrera, F.; Cerasuolo, M.; Tomasin, A.; Canestrelli, P. La nebbia a Venezia nel quarantennio 1951–1990. Analisi comparata degli andamenti di visibilità, pressione, temperatura e vento. Istituto Veneto di Scienze, Lettere ed Arti, Commissione di studio dei provvedimenti per la conservazione e difesa della laguna e della città di Venezia. *Rapp. Studi* **1995**, *12*, 235–271.
27. Dorigo, L. Ufficio idrografico. La laguna di Grado e le sue foci: Ricerche e rilievi idrografici. *Magistr. Alle Acque* **1965**, *155*, 231.
28. Polli, S. *Tabelle di Previsione Delle Maree per Trieste e L'Adriatico Settentrionale per L'anno 1971*; Istituto Sperimentale Talassografico "Francesco Vercelli": Trieste, Italy, 1970.
29. Dal Cin, R.; Simeoni, U. A model for determining the classification, vulnerability and risk in the southern coastal zone of the Marche (Italy). *J. Coast Res.* **1994**, *8*, 18–29.
30. Cavaleri, L.; Bergamasco, L.; Bertotti, L.; Bianco, L.; Drago, M.; Iovenitti, L.; Lavagnini, A.; Liberatore, G.; Martorelli, S.; Mattioli, F.; et al. Wind and waves in the northern Adriatic Sea. *Il Nuovo Cimento C* **1996**, *19*, 1–36. [CrossRef]
31. Meteoblue. Available online: https://content.meteoblue.com/it/research-development/case-studies/bora-wind-study (accessed on 26 July 2022).
32. Menegoni, N.; Giordan, D.; Perotti, C.; Tannant, D.D. Detection and geometric characterization of rock mass discontinuities using a 3D high-resolution digital outcrop model generated from RPAS imagery—Ormea rock slope, Italy. *Eng. Geol.* **2019**, *252*, 145–163. [CrossRef]
33. Devoto, S.; Macovaz, V.; Mantovani, M.; Soldati, M.; Furlani, S. Advantages of using UAV Digital Photogrammetry in the study of slow-moving coastal landslides. *Remote Sens.* **2020**, *12*, 3566. [CrossRef]
34. Paronuzzi, P.; Bolla, A. Gravity-induced rock mass damage related to large en masse rockslides: Evidence from Vajont. *Geomorphology* **2015**, *234*, 28–53. [CrossRef]
35. Paronuzzi, P.; Bolla, A. Gravity-induced fracturing in large rockslides: Possible evidence from Vajont. In *Engineering Geology for Society and Territory: Landslide Processes*; Lollino, G., Giordan, D., Crosta, G.B., Corominas, J., Azzam, R., Wasowski, J., Sciarra, N., Eds.; Springer: Berlin/Heidelberg, Germany, 2015; pp. 213–216.
36. Bolla, A.; Paronuzzi, P. Geomechanical field survey to identify an unstable rock slope: The Passo della Morte case history (NE Italy). *Rock Mech. Rock Eng.* **2020**, *53*, 1521–1544. [CrossRef]
37. Paronuzzi, P.; Bolla, A. In-depth field survey of a rockslide detachment surface to recognise the occurrence of gravity-induced cracking. *Eng. Geol.* **2022**, *302*, 106636. [CrossRef]
38. Brooke-Holland, L. *Unmanned Aerial Vehicles (Drones): An Introduction*; House of Commons Library: London, UK, 2012.
39. Francioni, M.; Salvini, R.; Stead, D.; Coggan, J. Improvements in the integration of remote sensing and rock slope modelling. *Nat. Hazards* **2018**, *90*, 975–1004. [CrossRef]
40. Giordan, D.; Hayakawa, Y.; Nex, F.; Remondino, F.; Tarolli, P. Review article: The use of remotely piloted aircraft systems (RPASs) for natural hazards monitoring and management. *Nat. Hazards Earth Syst. Sci.* **2018**, *18*, 1079–1096. [CrossRef]
41. Yao, H.; Qin, R.; Chen, X. Unmanned Aerial Vehicle for Remote Sensing Applications-A Review. *Remote Sens.* **2019**, *11*, 1443. [CrossRef]
42. Giordan, D.; Adams, M.S.; Aicardi, I.; Alicandro, M.; Allasia, P.; Baldo, M.; De Berardinis, P.; Dominici, D.; Godone, D.; Hobbs, P.; et al. The use of unmanned aerial vehicles (UAVs) for engineering geology applications. *Bull. Eng. Geol. Environ.* **2020**, *79*, 3437–3481. [CrossRef]
43. Colica, E.; D'Amico, S.; Iannucci, R.; Martino, S.; Gauci, A.; Galone, L.; Galea, P.; Paciello, A. Using unmanned aerial vehicle photogrammetry for digital geological surveys: Case study of Selmun promontory, northern of Malta. *Env. Earth Sci.* **2021**, *80*, 551. [CrossRef]
44. Tavani, S.; Billi, A.; Corradetti, A.; Mercuri, M.; Bosman, A.; Cuffaro, M.; Seers, T.; Carminati, E. Smartphone assisted fieldwork: Towards the digital transition of geoscience fieldwork using LiDAR-equipped iPhones. *Earth-Sci. Rev.* **2022**, *227*, 103969. [CrossRef]
45. Sturzenegger, M.; Stead, D. Close-range terrestrial digital photogrammetry and terrestrial laser scanning for discontinuity characterization on rock cuts. *Eng. Geol.* **2009**, *106*, 163–182. [CrossRef]
46. Xu, W.; Zhang, Y.; Li, X.; Wang, X.; Ma, F.; Zhao, J.; Zhang, Y. Extraction and statistics of discontinuity orientation and trace length from typical fractured rock mass: A case study on the Xinchang underground research laboratory site, China. *Eng. Geol.* **2020**, *269*, 105553. [CrossRef]
47. Riquelme, A.J.; Abellán, A.; Tomás, R. Characterization of rock slopes through slope mass rating using 3D point clouds. *Int. J. Rock Mech. Min. Sci.* **2016**, *84*, 165–176. [CrossRef]
48. Kong, D.; Saroglou, C.; Wu, F.; Li, B. Development and application of UAV-SfM photogrammetry for quantitative characterization of rock mass discontinuities. *Int. J. Rock Mech. Min. Sci.* **2021**, *141*, 104729. [CrossRef]
49. Riquelme, A.J.; Abellán, A.; Tomás, R. Discontinuity spacing analysis in rock masses using 3D point clouds. *Eng. Geol.* **2015**, *195*, 185–195. [CrossRef]
50. Riquelme, A.J. Discontinuity Set Extractor (DSE). Available online: https://personal.ua.es/en/ariquelme/discontinuity-set-extractor-software.html (accessed on 9 May 2022).
51. Herrero, M.-J.; Pérez-Fortes, A.P.; Escavy, J.I.; Insua-Arévalo, J.M.; De la Horra, R.; López-Acevedo, F.; Trigos, L. 3D model generated from UAV photogrammetry and semi-automatic rock mass characterization. *Comput. Geosci.* **2022**, *163*, 105121. [CrossRef]

52. Riquelme, A.J.; Abellán, A.; Tomás, R.; Jaboyedoff, M. A new approach for semi-automatic rock mass joints recognition from 3D point clouds. *Comput. Geosci.* **2014**, *68*, 38–52. [CrossRef]
53. Bolla, A.; Beinat, A.; Paronuzzi, P.; Peloso, C. Combined field and Structure from Motion survey to identify rock discontinuity sets of a shallow rockslide. *IOP Conf. Ser. Earth Environ. Sci.* **2021**, *906*, 12103. [CrossRef]
54. Marinos, P.; Hoek, E. Estimating the geotechnical properties of heterogeneous rock masses such as Flysch. *Bull. Eng. Geol. Env.* **2001**, *60*, 85–92. [CrossRef]
55. Marinos, P.; Marinos, V.; Hoek, E. The Geological Strength Index (GSI): A characterization tool for assessing engineering properties for rock masses. In *Proceedings of the International Workshop on Rock Mass Classification for Underground Mining, Vancouver, BC, Canada, 31 May 2007*; Mark, C., Pakalnis, R., Tuchman, R.J., Eds.; US Department of Health and Human Services: Pittsburgh, PA, USA, 2007; pp. 1248–1258.
56. Marinos, V. Tunnel behaviour and support associated with the weak rock masses of flysch. *J. Rock Mech. Geotech. Eng.* **2014**, *6*, 227–239. [CrossRef]
57. Gomez-Gutierrez, A.; Goncalves, G.R. Surveying coastal cliffs using two UAV platforms (multirotor and fixed-wing) and three different approaches for the estimation of volumetric changes. *Int. J. Remote Sens.* **2020**, *41*, 8143–8175. [CrossRef]
58. Barlow, J.; Gilham, J.; Ibarra Cofra, I. Kinematic analysis of sea cliff stability using UAV photogrammetry. *Int. J. Remote Sens.* **2017**, *38*, 2464–2479. [CrossRef]
59. Mancini, F.; Castagnetti, C.; Rossi, P.; Dubbini, M. An Integrated Procedure to Assess the Stability of Coastal Rocky Cliffs: From UAV Close-Range Photogrammetry to Geomechanical Finite Element Modeling. *Remote Sens.* **2017**, *12*, 1235. [CrossRef]
60. Riddick, S.N.; Schmidt, D.A.; Deligne, N.I. An analysis of terrain properties and the location of surface scatterers from persistent scatterer interferometry. *ISPRS J. Photogramm. Remote Sens.* **2012**, *73*, 50–57. [CrossRef]
61. Wasowski, J.; Bovenga, F. Investigating landslides and unstable slopes with satellite Multi Temporal Interferometry: Current issues and future perspectives. *Eng. Geol.* **2014**, *174*, 103–138. [CrossRef]
62. Li, W.; Zhan, W.; Lu, H.; Xu, Q.; Pei, X.; Wang, D.; Huang, R.; Ge, D. Precursors to large rockslides visible on optical remote-sensing images and their implications for landslide early detection. *Landslides* **2022**. [CrossRef]
63. Corradetti, A.; Seers, T.; Mercuri, M.; Calligaris, C.; Busetti, A.; Zini, L. Benchmarking Different SfM-MVS Photogrammetric and iOS LiDAR Acquisition Methods for the Digital Preservation of a Short-Lived Excavation: A Case Study from an Area of Sinkhole Related Subsidence. *Remote Sens.* **2022**, *14*, 5187. [CrossRef]